IAEA-TECDOC-1907

IAEA TECDOC SERIES

IAEA-TECDOC-1907

Benchmarking of Computational Fluid Dynamics Codes for Fuel Assembly Design

Results of a Coordinated Research Project

IAEA
International Atomic Energy Agency

IAEA SAFETY STANDARDS AND RELATED PUBLICATIONS

IAEA SAFETY STANDARDS

Under the terms of Article III of its Statute, the IAEA is authorized to establish or adopt standards of safety for protection of health and minimization of danger to life and property, and to provide for the application of these standards.

The publications by means of which the IAEA establishes standards are issued in the **IAEA Safety Standards Series**. This series covers nuclear safety, radiation safety, transport safety and waste safety. The publication categories in the series are **Safety Fundamentals**, **Safety Requirements** and **Safety Guides**.

Information on the IAEA's safety standards programme is available on the IAEA Internet site

http://www-ns.iaea.org/standards/

The site provides the texts in English of published and draft safety standards. The texts of safety standards issued in Arabic, Chinese, French, Russian and Spanish, the IAEA Safety Glossary and a status report for safety standards under development are also available. For further information, please contact the IAEA at: Vienna International Centre, PO Box 100, 1400 Vienna, Austria.

All users of IAEA safety standards are invited to inform the IAEA of experience in their use (e.g. as a basis for national regulations, for safety reviews and for training courses) for the purpose of ensuring that they continue to meet users' needs. Information may be provided via the IAEA Internet site or by post, as above, or by email to Official.Mail@iaea.org.

RELATED PUBLICATIONS

The IAEA provides for the application of the standards and, under the terms of Articles III and VIII.C of its Statute, makes available and fosters the exchange of information relating to peaceful nuclear activities and serves as an intermediary among its Member States for this purpose.

Reports on safety in nuclear activities are issued as **Safety Reports**, which provide practical examples and detailed methods that can be used in support of the safety standards.

Other safety related IAEA publications are issued as **Emergency Preparedness and Response** publications, **Radiological Assessment Reports**, the International Nuclear Safety Group's **INSAG Reports**, **Technical Reports** and **TECDOCs**. The IAEA also issues reports on radiological accidents, training manuals and practical manuals, and other special safety related publications.

Security related publications are issued in the **IAEA Nuclear Security Series**.

The **IAEA Nuclear Energy Series** comprises informational publications to encourage and assist research on, and the development and practical application of, nuclear energy for peaceful purposes. It includes reports and guides on the status of and advances in technology, and on experience, good practices and practical examples in the areas of nuclear power, the nuclear fuel cycle, radioactive waste management and decommissioning.

BENCHMARKING OF COMPUTATIONAL FLUID DYNAMICS CODES FOR FUEL ASSEMBLY DESIGN

The following States are Members of the International Atomic Energy Agency:

AFGHANISTAN
ALBANIA
ALGERIA
ANGOLA
ANTIGUA AND BARBUDA
ARGENTINA
ARMENIA
AUSTRALIA
AUSTRIA
AZERBAIJAN
BAHAMAS
BAHRAIN
BANGLADESH
BARBADOS
BELARUS
BELGIUM
BELIZE
BENIN
BOLIVIA, PLURINATIONAL STATE OF
BOSNIA AND HERZEGOVINA
BOTSWANA
BRAZIL
BRUNEI DARUSSALAM
BULGARIA
BURKINA FASO
BURUNDI
CAMBODIA
CAMEROON
CANADA
CENTRAL AFRICAN REPUBLIC
CHAD
CHILE
CHINA
COLOMBIA
CONGO
COSTA RICA
CÔTE D'IVOIRE
CROATIA
CUBA
CYPRUS
CZECH REPUBLIC
DEMOCRATIC REPUBLIC OF THE CONGO
DENMARK
DJIBOUTI
DOMINICA
DOMINICAN REPUBLIC
ECUADOR
EGYPT
EL SALVADOR
ERITREA
ESTONIA
ESWATINI
ETHIOPIA
FIJI
FINLAND
FRANCE
GABON
GEORGIA
GERMANY
GHANA
GREECE
GRENADA
GUATEMALA
GUYANA
HAITI
HOLY SEE
HONDURAS
HUNGARY
ICELAND
INDIA
INDONESIA
IRAN, ISLAMIC REPUBLIC OF
IRAQ
IRELAND
ISRAEL
ITALY
JAMAICA
JAPAN
JORDAN
KAZAKHSTAN
KENYA
KOREA, REPUBLIC OF
KUWAIT
KYRGYZSTAN
LAO PEOPLE'S DEMOCRATIC REPUBLIC
LATVIA
LEBANON
LESOTHO
LIBERIA
LIBYA
LIECHTENSTEIN
LITHUANIA
LUXEMBOURG
MADAGASCAR
MALAWI
MALAYSIA
MALI
MALTA
MARSHALL ISLANDS
MAURITANIA
MAURITIUS
MEXICO
MONACO
MONGOLIA
MONTENEGRO
MOROCCO
MOZAMBIQUE
MYANMAR
NAMIBIA
NEPAL
NETHERLANDS
NEW ZEALAND
NICARAGUA
NIGER
NIGERIA
NORTH MACEDONIA
NORWAY
OMAN
PAKISTAN
PALAU
PANAMA
PAPUA NEW GUINEA
PARAGUAY
PERU
PHILIPPINES
POLAND
PORTUGAL
QATAR
REPUBLIC OF MOLDOVA
ROMANIA
RUSSIAN FEDERATION
RWANDA
SAINT LUCIA
SAINT VINCENT AND THE GRENADINES
SAN MARINO
SAUDI ARABIA
SENEGAL
SERBIA
SEYCHELLES
SIERRA LEONE
SINGAPORE
SLOVAKIA
SLOVENIA
SOUTH AFRICA
SPAIN
SRI LANKA
SUDAN
SWEDEN
SWITZERLAND
SYRIAN ARAB REPUBLIC
TAJIKISTAN
THAILAND
TOGO
TRINIDAD AND TOBAGO
TUNISIA
TURKEY
TURKMENISTAN
UGANDA
UKRAINE
UNITED ARAB EMIRATES
UNITED KINGDOM OF GREAT BRITAIN AND NORTHERN IRELAND
UNITED REPUBLIC OF TANZANIA
UNITED STATES OF AMERICA
URUGUAY
UZBEKISTAN
VANUATU
VENEZUELA, BOLIVARIAN REPUBLIC OF
VIET NAM
YEMEN
ZAMBIA
ZIMBABWE

The Agency's Statute was approved on 23 October 1956 by the Conference on the Statute of the IAEA held at United Nations Headquarters, New York; it entered into force on 29 July 1957. The Headquarters of the Agency are situated in Vienna. Its principal objective is "to accelerate and enlarge the contribution of atomic energy to peace, health and prosperity throughout the world".

IAEA-TECDOC-1907

BENCHMARKING OF COMPUTATIONAL FLUID DYNAMICS CODES FOR FUEL ASSEMBLY DESIGN

RESULTS OF A COORDINATED RESEARCH PROJECT

INTERNATIONAL ATOMIC ENERGY AGENCY
VIENNA, 2020

For further information on this publication, please contact:

Nuclear Power Technology Development Section
International Atomic Energy Agency
Vienna International Centre
PO Box 100
1400 Vienna, Austria
Email: Official.Mail@iaea.org

Printed by the IAEA in Austria
May 2020

IAEA Library Cataloguing in Publication Data

Names: International Atomic Energy Agency.
Title: Benchmarking of computational fluid dynamics codes for fuel assembly design / International Atomic Energy Agency.
Description: Vienna : International Atomic Energy Agency, 2020. | Series: IAEA TECDOC series, ISSN 1011–4289 ; no. 1907 | Includes bibliographical references.
Identifiers: IAEAL 20-01312 | ISBN 978–92–0–106820–0 (paperback : alk. paper) |
ISBN 978–92–0–106920–7 (pdf)
Subjects: LCSH: Nuclear fuel elements — Computer programs. | Water cooled reactors. | Computational fluid dynamics.

FOREWORD

The IAEA organizes coordinated research projects (CRPs) to complement, and share knowledge from, research on a common topic conducted by Member State organizations. The implementation of a CRP sometimes includes an experimental investigation of interesting phenomena and simulation of the experiment with computer codes. Activities within the framework of the Technical Working Group on Advanced Technologies for Light Water Reactors (TWG-LWR) are conducted in a project within the IAEA's subprogramme on nuclear power reactor technology development. One of the activities recommended by the TWG-LWR was a CRP on Application of Computational Fluid Dynamics (CFD) Codes for Nuclear Power Plant Design.

Advanced nuclear power plants are now offered by various vendors, and in recent years these plants have increasingly used CFD codes in their design. This recently completed CRP addressed the application of CFD computer codes to the process of optimizing the design of water cooled nuclear power plants. Following several initiatives within the IAEA for which CFD codes have been applied to a wide range of situations of interest in nuclear reactor technology, this CRP aimed to contribute to a consistent application of CFD codes and their models in the design of nuclear power plant components important to safety.

This publication provides a description of the Omni Flow Experimental Loop (OFEL) test facility, used to provide benchmark experiments related to the phenomena of fuel assembly spacer grid induced flow mixing; the calculation results from six participants using CFD codes and methods; and conclusions drawn from the comparison of CFD results with experimental measurements. The work was done within the framework of the CRP.

The IAEA expresses its appreciation for the generous contribution of experimental data and insights, and for assembling participants' results in drafting this report, by the Korean Atomic Energy Research Institute (KAERI) and acknowledges the efforts and assistance provided by the contributors listed at the end of this publication. The IAEA officer responsible for this publication was M. Krause of the Division of Nuclear Power.

CONTENTS

1. INRODUCTION

The International Atomic Energy Agency (IAEA) fosters international cooperation on technology development for improved safety of water cooled reactors (WCRs) with the goals to increase fundamental understanding and improve the modelling tools. Benchmarking and validation of computer codes for WCR design and safety analyses is an ongoing activity to facilitate international cooperative research and promote information exchange on computer codes for WCR design and safety analyses. The objective is to enhance the analysis capabilities of the participants and the effective use of their resources in Member States. Along with focused code comparison exercises against experiments, these collaborations provide participants from R&D, plant operators, and regulatory bodies valuable data against which analysis methods and codes can be benchmarked in the future.

A coordinated research project (CRP) on *Application of Computational Fluid Dynamics (CFD) Codes to Nuclear Power Plant Design* was conducted from 2012 to 2018 to benchmark CFD codes, model options and methods against 'CFD quality' experimental data under single phase flow conditions. This report documents the work performed and results obtained by seven participating institutes from six Member States, all with currently operating WCRs.

1.1. BACKGROUND

The use of single phase CFD codes for nuclear applications has evolved from the subchannel analysis codes developed in the 1980s. The ability of CFD to simulate the three dimensional aspects of various NPP phenomena, including pressurized thermal shock (PTS), boron dilution, thermal fatigue, hydrogen distribution in containments, hot leg temperature homogeneities, etc., has brought the technology to the forefront of NPP safety and design considerations. The development, verification and validation of CFD codes in respect to NPP design necessitates further modelling work on the complex physical processes involved, and on the development of the efficient numerical schemes needed to solve the basic equations in an efficient manner, including advanced turbulence modelling.

At an early meeting of the CRP on the application of CFD for nuclear power plant design, it was decided to launch several benchmark exercises during 2015. To this purpose, two organizations (HZDR and KAERI) made available valuable experimental data. The present report is dedicated to the four Omni Flow Experimental Loop (OFEL) test facility benchmarks, proposed by KAERI, and for which data from two experiments related to the phenomena of fuel assembly spacer grid induced flow mixing were provided. OFEL is a 2:1 linear scale transparent model of a 4x4 PWR rod bundle assembly, with detailed flow velocity, turbulence and heat transfer measurements.

The fuel assembly loaded into a nuclear reactor core is generally of a square or triangular rod bundle arrangement in which the coolant is driven axially through the sub–channels formed between neighboring fuel rods. The rod–to–rod clearance is maintained by a spacer grid or by means of a helical wire wrap. The pitch–to–diameter (P/D) ratio and the fuel spacer/wrap design significantly affect the coolant flow distribution in the bundle. Here, P and D indicate the pitch between rods and the rod diameter, respectively. The P/D ratio of a fuel bundle and the spacer grid geometry have a strong influence on the thermal–hydraulic characteristics, including the maximum fuel temperature, the conditions leading to critical heat flux (CHF), and the pressure drop through the bundle. An understanding of the detailed structure of flow mixing and heat transfer in a fuel rod bundle geometry is therefore an important aspect of reactor core design, both in terms of the reactor's reliable operation, and for optimum power extraction.

1.2. OBJECTIVE

The objective of this CFD benchmark against tests performed in the OFEL facility was to provide CFD practitioners with high quality datasets of relevance to flow mixing and heat transfer enhancement in a PWR–type fuel assembly. The experiments were carried out to quantify flow mixing and heat transfer in regular (P/D = 1.35) and thigh–lattice (P/D = 1.08) rod–bundle geometries. For both test geometries, the rod bundle is a square 4x4 rod array in which a twist–vane spacer grid is employed to promote flow mixing.

1.3. SCOPE

The focus of the benchmark was on the downstream region after the spacer grid. The comparisons between the experimental measurements and the CFD calculations are hence focused on the average velocity, the fluctuating velocity (turbulence), and local cladding temperatures in this region. This document presents the results from these benchmarks.

The CFD codes used in the KAERI bundle benchmarks are ANSYS CFX [1], OpenFOAM [2], STAR–CCM+ [3] and TrioCFD [4]. Both RANS turbulence models and Large Eddy Simulation were used to simulate flow turbulence in the rod bundle. The mesh types are tetrahedral, polyhedral, Hexa–dominant or hybrid (tetra+hexa). The total number of computational cells varied between 8 million (minimum) and 280 million (maximum).

1.4. STRUCTURE

This technical document (TECDOC) provides a description of the OFEL test facility, used to provide benchmark experiments, the calculation results from seven participants and conclusions drawn from comparison of CFD results with experimental measurements.

Section 1 recalls the background, the objectives and scope of the benchmark exercises as well as the organization of this TECDOC. The experimental facility, test sections and measurements available are described in Section 2. Important statistics of the different contributions are given for each participant in precise form (Section 3), before a synthesis of the results is presented in Section 4. Finally, conclusions and some guidelines for future CFD simulations, drawn from these benchmarks are presented in Section 6.

2. OFEL ROD–BUNDLE EXPERIMENTS (KAERI)

2.1. INTRODUCTION

Korea Atomic Energy Research Institute (KAERI) has developed a twist–vane grid to enhance thermal–hydraulic performance of PWR fuel assembly and a dual–cooled annular fuel for the power uprate in the OPR1000 reactor. The twist–vane grid was developed to enhance the crossflow mixing between adjacent subchannels by creating a swirl mixing within the subchannel.

Figure 1 illustrates the twist–vane grid consisting of triangular vane supports and pairs of polygonal vanes that are integrally formed on the top edges of the grid straps. The dual–cooled fuel for the OPR1000 was targeted to increase the reactor power by 20 %, as well as reduce the fuel–pellet temperature by more than 30 % without a change to the reactor components other than the fuel. The dual–cooled fuel is configured to allow the coolant flow through the inner channel as well as the outer channel. A 12x12 dual–cooled fuel assembly shown in Fig. 2. was proposed for the OPR1000 core. This fuel assembly was designed to be structurally compatible with the 16x16 cylindrical solid fuel assembly by maintaining the same array size and the guide tubes for the same locations.

The dual–cooled fuel array comes to exhibit a smaller P/D ratio, i.e., 1.08, than a cylindrical solid fuel array with P/D = 1.35 owing to a larger outer cladding diameter. This change results in a significant difference in the characteristics of the flow–mixing phenomena, the pressure drop and the temperature distribution between the dual–cooled annular and conventional cylindrical solid fuel bundle designs. Consequently, detailed thermal–hydraulic analyses and experiments are necessary to assess the applicability of the dual–cooled fuel concept to the OPR1000 core. In particular, experiments were conducted to evaluate flow mixing between adjacent subchannels and heat transfer in a tight lattice rod bundle (P/D = 1.08) as well as in regular rod bundle (P/D = 1.35).

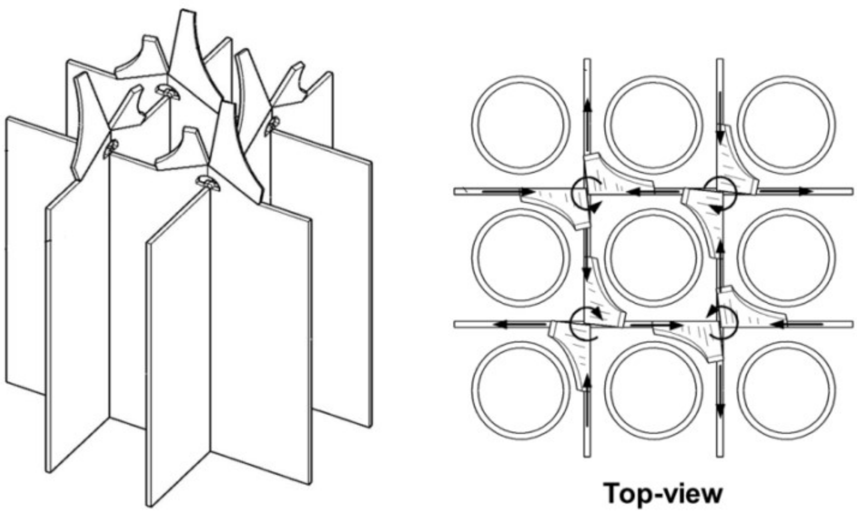

FIG. 1. Schematic of twist–vane grid (Reproduced courtesy of KAERI [5]).

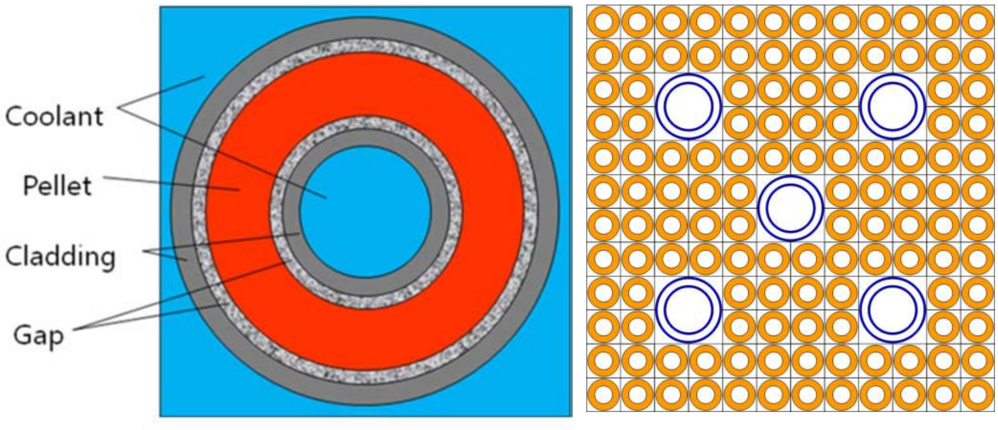

FIG. 2. Schematic of dual–cooled annular fuel and 12x12 fuel assembly for the OPR1000 core (Reproduced courtesy of KAERI [6]).

The KAERI experiment was carried out to quantify flow mixing and heat transfer in regular (P/D = 1.35) and thigh–lattice (P/D = 1.08) rod–bundle geometries. For both test geometries, the rod bundle is a square 4x4 rod array in which a twist–vane spacer grid is employed to promote flow mixing. Table 1 shows the test matrix in concise form, together with the experimental conditions.

TABLE 1. TEST MATRIX FOR FLOW MIXING AND HEAT TRANSFER EXPERIMENTS

Case ID	Category	P/D	Array	Spacer grid	Experimental outcomes
RB01	Isothermal flow (flow mixing)	1.35	4x4	Twist–vane	– Axial & lateral velocities in the sub–channel – Turbulent intensity and mixing parameters
RB02		1.08			
RB03	Thermal flow (heat transfer)	1.35			– Wall temperature – Fluid temperature
RB04		1.08			

The flow mixing experiments under isothermal conditions (RB01 and RB02) involve the measurement of velocity distributions in the subchannels using particle image velocimetry (PIV) and laser doppler velocimetry (LDV) techniques. Due to the influence of the mixing–vane space grid on the flow distribution, both axial and lateral velocities are measured in the sub–channels upstream and downstream of the spacer grid.

It is well known that the P/D ratio, and the mixing–vane spacer grid design, both have a strong influence, not only on the flow field but also on the thermal field within the rod bundle. The tight lattice configuration (with a small P/D ratio) can create a hot spot on the rod surface, which may result in local boiling, and thereby denigrating the CHF performance of the bundle. Consequently, the thermal experiments RB03 and RB04 were conducted to measure the surface temperatures of the heated rods, both for the regular and tight lattice configurations, together with the presence of the mixing–vane spacer grid. In the thermal experiments, the axial and circumferential variations of rod temperature are measured, together with the fluid temperature for the center subchannel.

Several organizations participating in this IAEA CRP have performed a CFD analysis to simulate the isothermal and thermal KAERI bundle tests. Six and five organizations submitted the CFD results for the isothermal and thermal benchmarks in a 4x4 rod bundle, respectively. This report is to synthesize the CFD results as well as to document the experimental works.

2.2.FLOW–MIXING EXPERIMENT

The OFEL facility has been built to measure the thermal–hydraulic characteristics of rod bundle flow. OFEL consists of a test section with a rod bundle geometry, a centrifugal water pump, a water storage tank and a flow meter, as shown in Fig. 3. The water temperature for testing is controlled by the immersion cartridge heater, and by a heat exchanger of air cooling connected to the water storage tank. Using a centrifugal pump, the water flows from the reservoir to the plenum at the lower part of the vertical test section. The water flow rate is controlled by the variable frequency drive (VFD) and is measured using the mass and turbine flow meters.

To measure the water temperature, a T–type thermocouple (Omega) is installed in the inlet plenum. All experimental data are collected using a commercial data acquisition system. As working fluid, de–mineralized water is used. To measure the flow velocities within the rod bundle, both PIV and LDV techniques are employed. For the PIV system (Dantec), the laser has dual cavities. For each cavity, the power, pulse rate and wavelength are 20 mJ, 1 kHz and 527 nm, respectively. A high–speed camera (Speed Sense 9072) can provide up to 2190 fps (frames/sec) at full resolution of a 1280×800 pixel matrix. For the LDV system set–up (MSE), the laser power and wavelength are 130 mW and 660 nm, respectively. The PIV set–up is displayed in Fig. 4.

The test section consists of a square housing, holder, rod bundle, fixing plate, rod support, and spacer grid with mixing vanes of generic design, as illustrated in Fig. 5. Two designs of the test section were employed in these tests: P/D = 1.35 and P/D = 1.08, to represent regular and tight lattice fuel bundles, respectively. The dimensions of the square housings are 142 mm × 142 mm for P/D = 1.35 and 112 mm × 112 mm for P/D = 1.08, respectively. For each rod bundle, the cylindrical rod is 2000 mm in length and 25.4 mm in diameter(D), each assembled using 10 unit rods made of Acetal resin (a type of plastic material). Downstream of the mixing–vane spacer grid, transparent FEP (fluorinated ethylene propylene) tubes of length 200 mm have been placed, each filled with water. As the refractive index of the FEP material (1.34) is quite similar to that of water (1.33), the optical distortion of the laser sheet through the FEP tube filled with water can be minimized. The rod supports are made of stainless steel (SS304) of 5 mm thickness and have been precisely machined using the EDM (electrical discharge machining) wire cutting process.

A 3D printing process was used to manufacture the spacer grids, each with its twist–vanes, as illustrated in Fig. 6. The material of the spacer grid is ABS (acrylonitrile butadiene styrene) and its thickness is 1.51 mm and 2.02 mm for P/D = 1.08 and 1.35, respectively. The spacer grid has been coated with black paint to minimize light reflection.

Figure 7 shows the cross–sectional view and measured region in the central subchannel of 4x4 rod bundle with the twist–vane grid for P/D = 1.35 and 1.08, respectively. The mean and RMS lateral velocity was measured using the PIV system in the central subchannel. The PIV measurements were taken at 1.4D, 3D, 6D, 10D, 14D and 20D downstream of the vane grid. The mean and RMS axial velocity was also measured using the LDV system in the center and rod–to–rod gap of the central subchannel. The LDV measurements were taken from 1.6D (40 mm) to 9.1D (230 mm) downstream of the vane grid. Figure 8 shows the coordinate system and measuring locations for the PIV and LDV systems. The origin of axial coordinate (z), i.e., z = 0, is placed at the top end of vane grid. The origin of lateral coordinates (x and y) is defined at the center of the central subchannel.

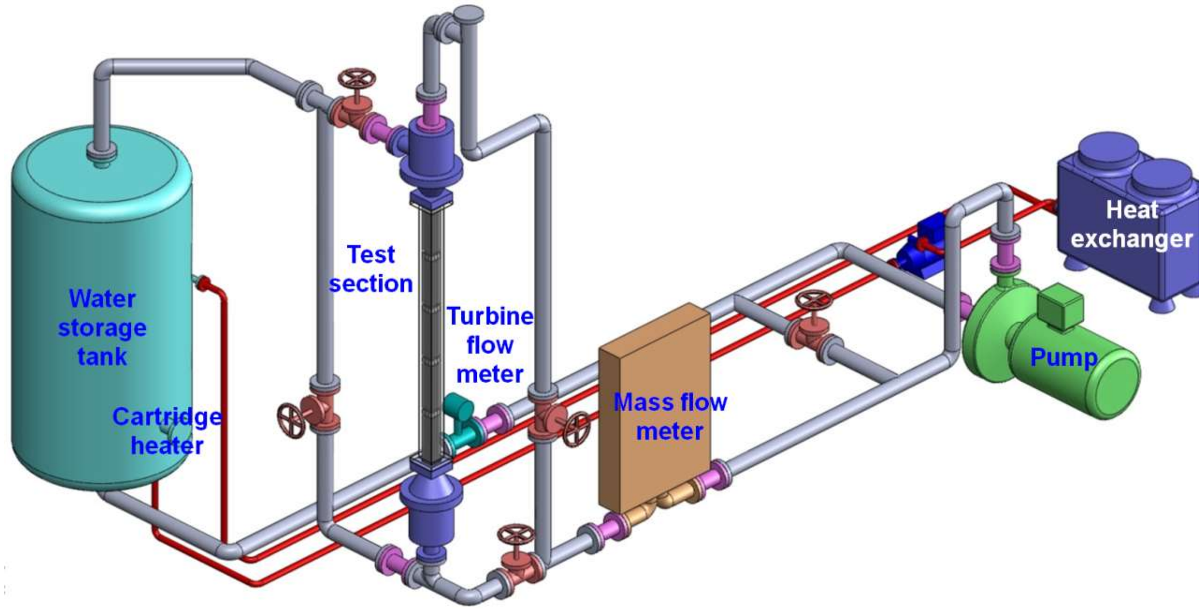

FIG. 3. Schematic of the OFEL test loop (Reproduced courtesy of KAERI [7]).

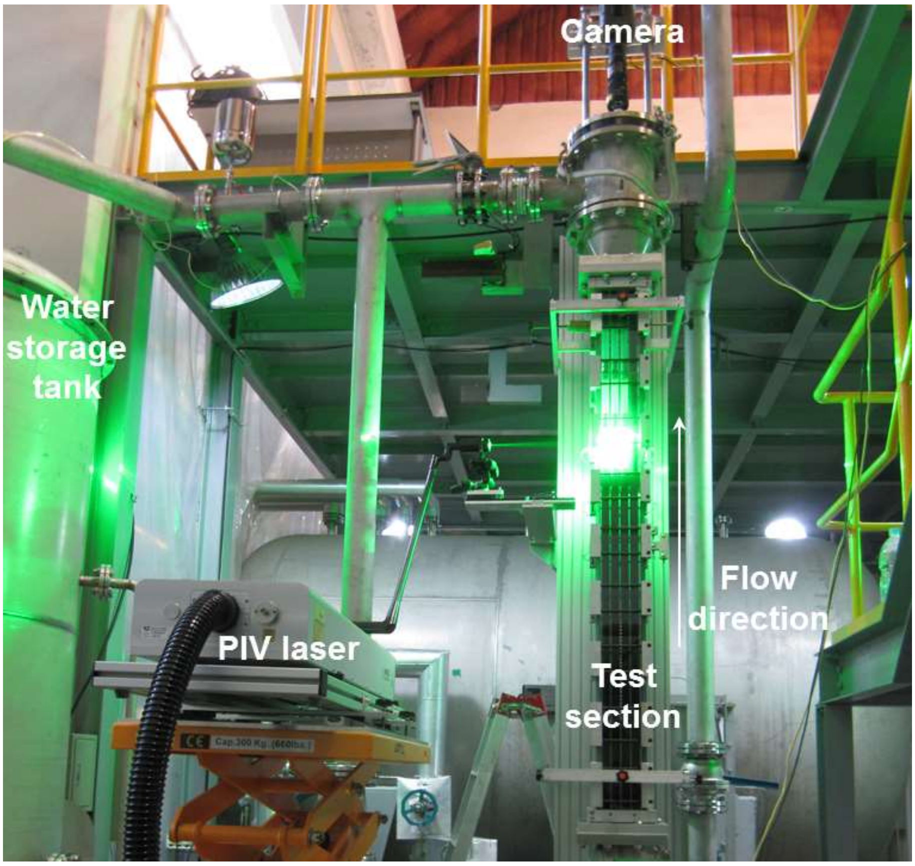

FIG. 4. Setup of the PIC system (Reproduced courtesy of KAERI [7]).

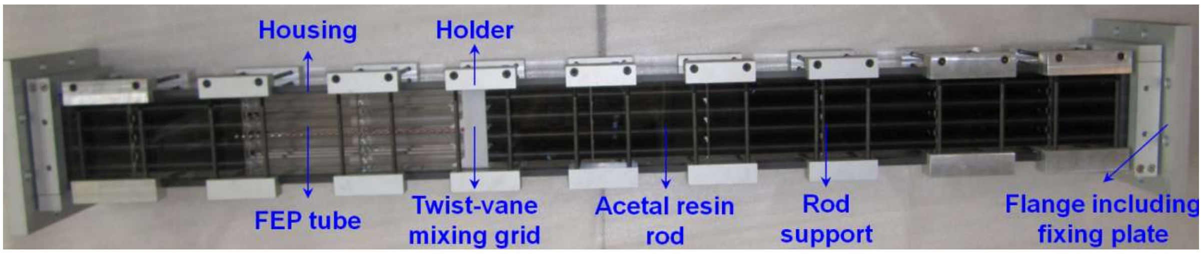

FIG. 5. Test section of 4x4 rod bundle with twist–vane grid (Reproduced courtesy of KAERI [7]).

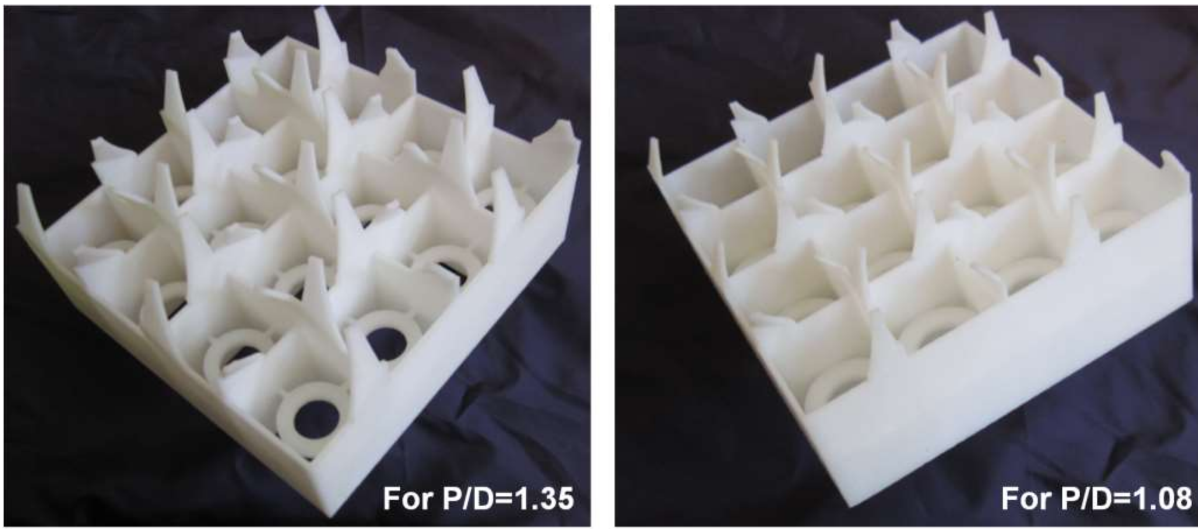

FIG. 6. Twist–vane grid manufactured by 3D printing technique (Reproduced courtesy of KAERI [6], [7]).

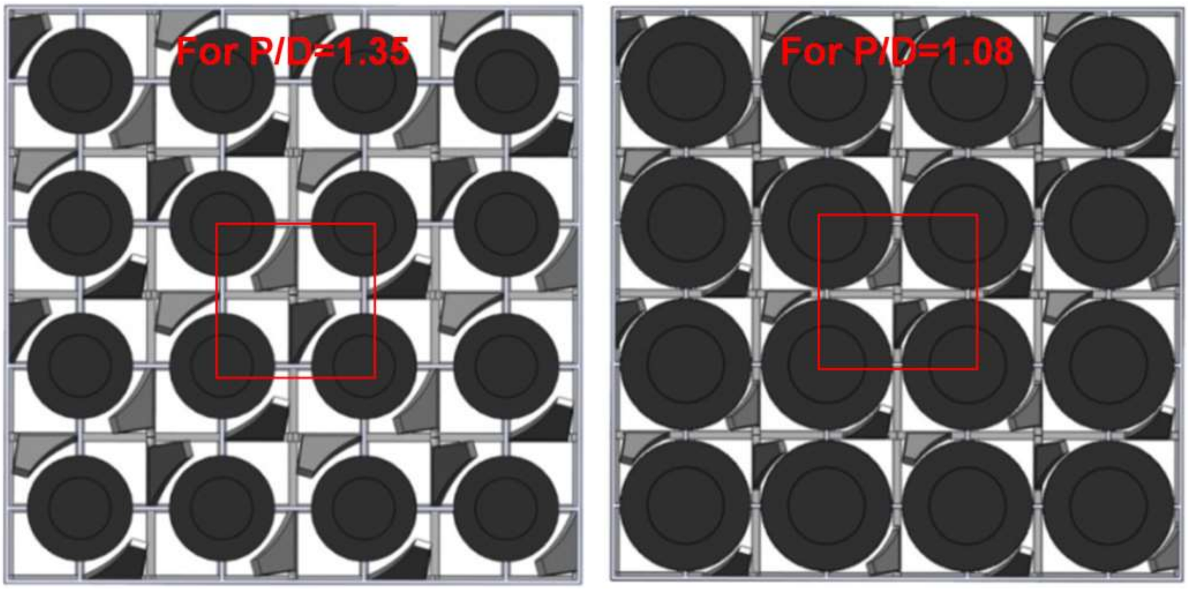

FIG. 7. Cross–sectional view of measurement regions for regular and tight lattice bundles (Reproduced courtesy of KAERI [6] [7]).

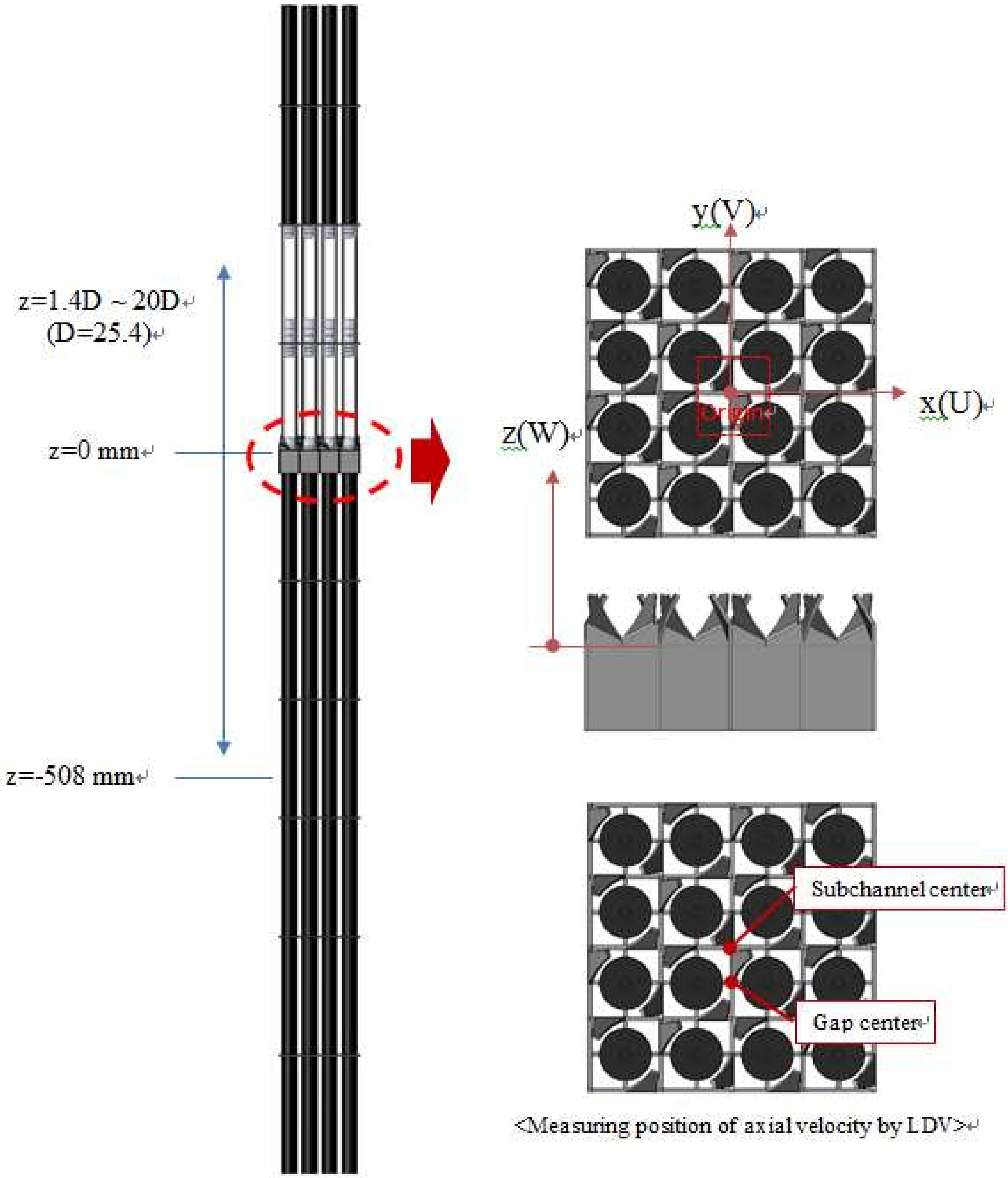

FIG. 8. Coordinate system and measuring locations.

The axial velocities were measured at a number of downstream locations using LDV. The measuring conditions are summarized as follows:

— Cut–off minimum speed: 0.5 m/s
— Cut–off maximum speed: 2.75 m/s
— Cut–off minimum SNR (signal–to–noise ratio): 2.0
— Average data collection rate: 8000 Hz
— Total number of acquired data points: 100000

The lateral velocities were measured using PIV and the measuring conditions are summarized as follows:

— System control
- Image map: 768x768 pixels
- Time between pulses: 200 μs
- Trigger rate: 1800 Hz
- No. of datasets: 6000

— Analysis methods
- Calculation: adaptive correlation method
- Initial interrogation area: 64x64 pixels
- Final interrogation area: 16x16 pixels
- Image overlap: 50 %

The mean and RMS velocity are obtained using statistical analysis as follows:

Mean velocity:
$$U = \frac{1}{N}\sum_{n=1}^{N} u_n \tag{1}$$

RMS velocity:
$$U_{rms} = \sqrt{\frac{\sum_{n=1}^{N}(u_n - U)^2}{N-1}} \tag{2}$$

where N is the number of measurement data.

The flow velocity at the inlet was measured at the upstream position 20D from the upper end of the mixing vane spacer grid. The velocity data were acquired along the lateral center line of the test section between the second and third rows of the 4x4 rod array. Figure 9 shows axial velocity distribution in central subchannel and neighboring subchannels at the inlet boundary (–20D) for the test bundles with P/D = 1.35 and 1.08. It can be confirmed that the axial velocity distribution at the inlet boundary is nearly uniform in inner subchannels.

Mean and RMS axial velocities at the center and gap of central subchannel are measured in the regular bundle (P/D = 1.35) as shown in Figs. 10 and 11. The mean axial velocity at the subchannel center in Fig. 10 appears to decrease near downstream of the grid (e.g., z < 2D) and continually increase further downstream. The mean axial velocity at the gap in Fig. 10 shows a double–peak just downstream of the grid (e.g., z < 3D) and decreases further downstream.

The RMS axial velocity in Fig. 11 continually decreases downstream of the grid. The RMS axial velocity at the subchannel center is higher than the measured one at the gap.

The mean and RMS axial velocities for tight lattice bundle (P/D = 1.08) were also measured at the center and gap of central subchannel as shown in Figs. 12 and 13. The mean axial velocity the subchannel center slightly decreases near downstream of the grid and increases to a far downstream value. The mean velocity at the gap appears to slightly increase near downstream of the grid but reaches at a constant value. It is noted that the variation of axial velocity for tight lattice bundle is smaller than the measured result for regular bundle. The measured RMS axial velocity in Fig. 13 shows a gradual decrease downstream of the grid and almost the same values for the subchannel center and gap.

The flow mixing pattern in the central subchannel is illustrated in Figs 14 and 15 for regular bundle (P/D = 1.35) and tight lattice bundle (P/D = 1.08), respectively. The lateral velocity vector for regular bundle and near downstream of the twist–vane grid (P/D = 1.35, z/D = 1.4) in Fig. 14 shows a large swirl in the central region and secondary swirl in the peripheral region near the gap. It also shows a strong crossflow in the gap between adjacent subchannels. Further downstream of the grid in regular bundle (P/D = 1.35, z/D = 6.0), a single circular swirl is measured in the central region and asymmetric crossflow in the gap.

The lateral velocity vector for tight lattice bundle and near downstream of the twist–vane grid (P/D = 1.08, z/D = 1.4) in Fig. 15 shows two elliptic swirls rotating in opposite direction and large crossflow in the gap. A single elliptic swirl is measured in the central region and small crossflow in the gap little far downstream of the grid in tight lattice bundle (P/D = 1.08, z/D = 6.0). The lateral velocity vectors were also measured at various locations downstream of the twist–vane grid and provided to the participants.

Figure 16 shows the mean lateral (vertical) velocity profiles along the horizontal centerline in the central subchannel for regular bundle (P/D = 1.35). A symmetric distribution can be observed in the vertical velocity profile due to the swirl pattern caused by the twist–vane grid. Double peaks are observed in the near downstream velocity profile, i.e., z/D = 1.4. The magnitude of vertical velocity decreases as it goes downstream of the vane grid. The maximum vertical velocity is 0.7 m/sec (46 % of bundle–flow velocity) near downstream of the grid (z/D = 1.4) and 0.2 m/sec far downstream (z/D = 20).

Figure 17 shows the RMS lateral velocity profiles along the horizontal centerline in the central subchannel for regular bundle (P/D = 1.35). The RMS velocity shows the peak value at the subchannel center (x = 0) and the low value in the gap (x < –15, x > 15). The RMS velocity near downstream (z/D = 1.4) is significantly higher than the results further downstream.

The mean crossflow velocity is measured in the left gap of central subchannel for regular bundle. The crossflow between adjacent subchannels occurs due to the twist vane.

Figure 18 shows the mean crossflow velocity (Um) measured at various axial locations downstream of the vane grid, e.g., z/D = 1.4, 3, 6, 10, 14, 20. The negative value indicates the crossflow from the central subchannel to the subchannel in the left side (outflow to the west direction). The crossflow velocity is high up to 0.6 m/sec (40 % of bundle–flow velocity) near downstream of the grid (z/D < 3) and rapidly decreases below 0.2 m/sec little far downstream (z/D > 10).

Figure 19 shows the mean lateral (vertical) velocity profiles along the horizontal centerline in the central subchannel for tight lattice bundle (P/D = 1.08). A symmetric distribution can be observed in the vertical velocity profile due to the swirl pattern caused by the twist–vane grid. The magnitude of vertical velocity decreases rapidly as it goes downstream of the vane grid. The maximum vertical velocity is 0.35 m/sec (23 % of bundle–flow velocity) near downstream of the grid (z/D = 1.4) and 0.1 m/sec a little downstream (z/D = 3). It is therefore noted that the magnitude of swirl in tight lattice bundle is significantly smaller than the regular–bundle case.

Figure 20 shows the RMS lateral velocity profiles along the horizontal centerline in the central subchannel for tight lattice bundle (P/D = 1.08). The RMS velocity shows the peak value at the subchannel center (x = 0) and the low value in the gap (x < –10, x > 10). The RMS velocity near downstream (z/D = 1.4 & 3) is significantly higher than the results further downstream (z/D > 6).

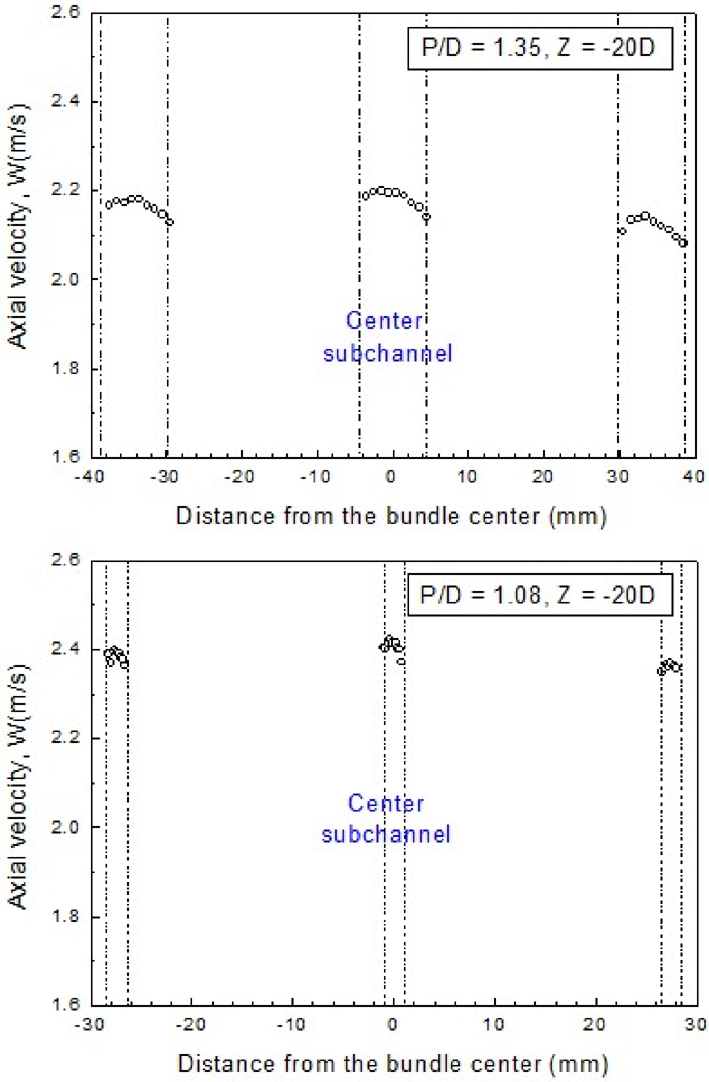

FIG. 9. Axial velocity distribution at the inlet boundary (20D upstream of spacer grid).

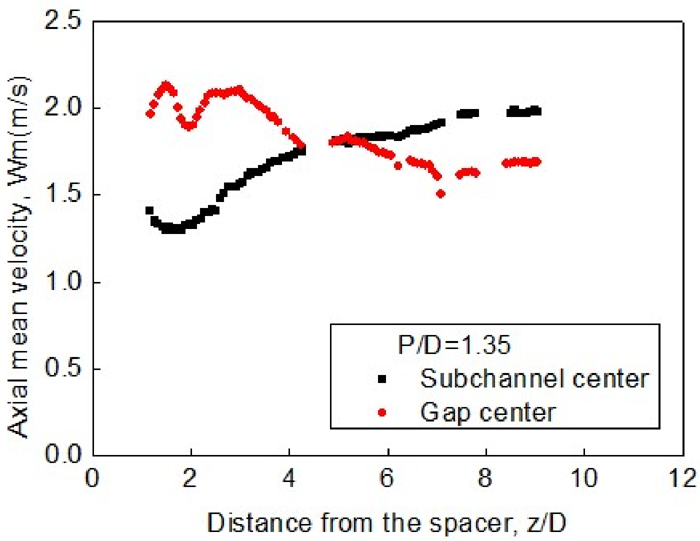

FIG. 10. Mean axial velocity distribution in regular rod bundle (P/D = 1.35).

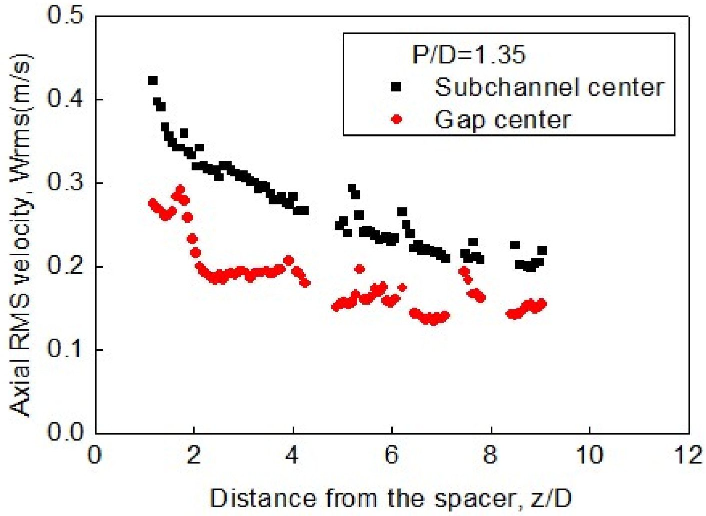

FIG. 11. RMS axial velocity distribution in regular rod bundle (P/D = 1.35).

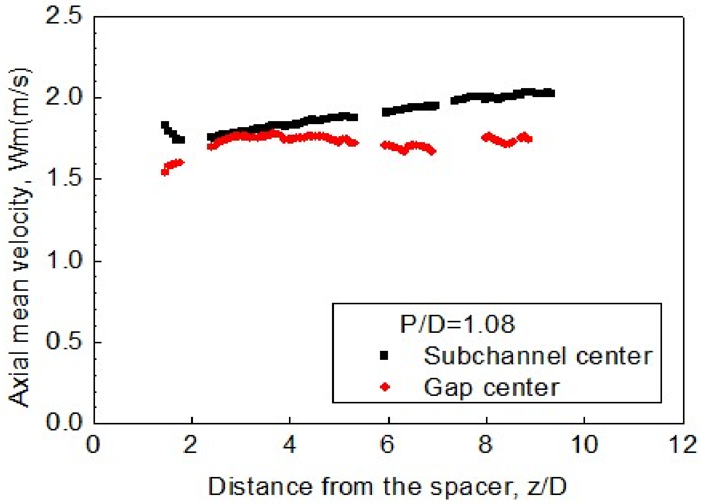

FIG. 12. Mean axial velocity distribution in tight lattice rod bundle (P/D = 1.08).

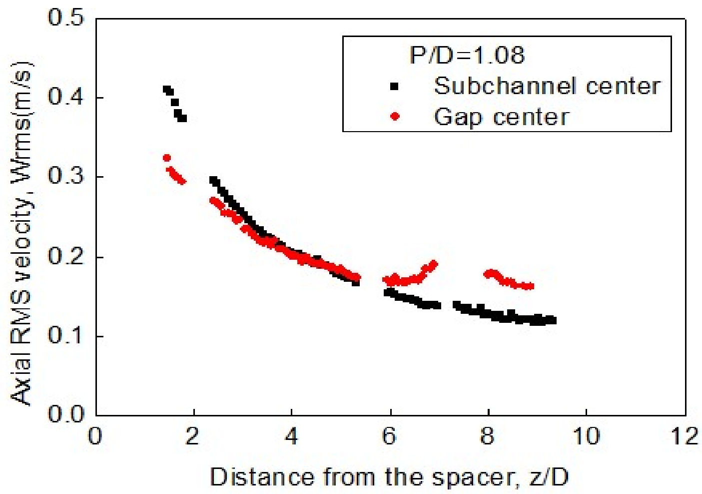

FIG. 13. RMS axial velocity distribution in tight lattice rod bundle (P/D = 1.08).

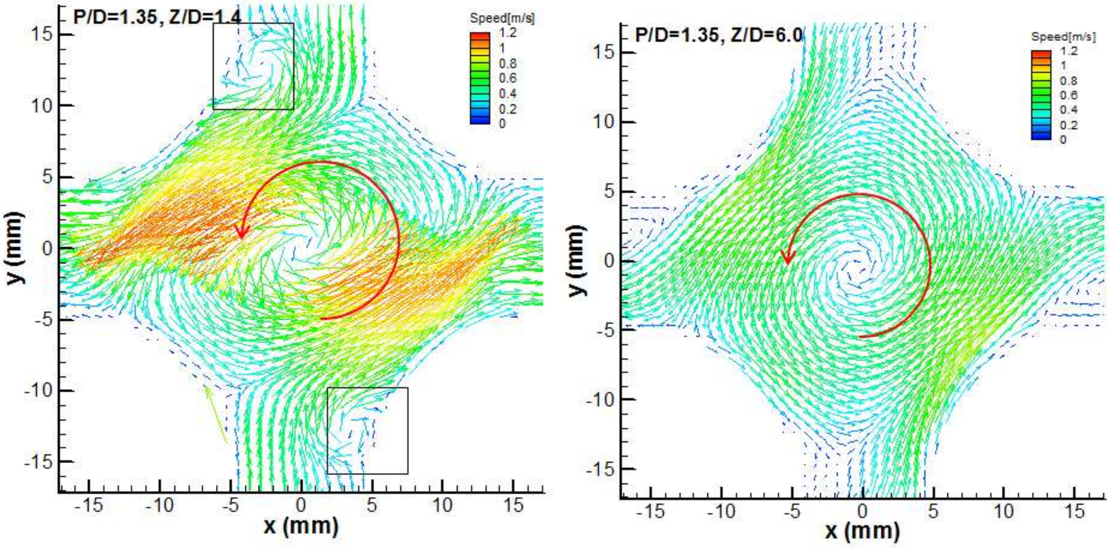

FIG. 14. Lateral velocity vector in the central subchannel of regular bundle (P/D = 1.35).

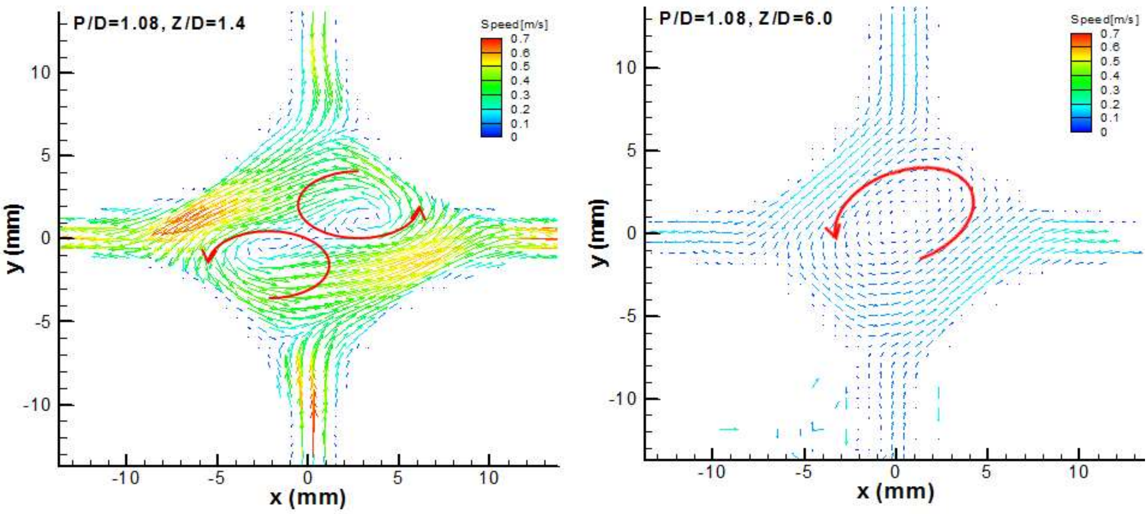

FIG. 15. Lateral velocity vector in the central subchannel of tight lattice bundle (P/D = 1.08).

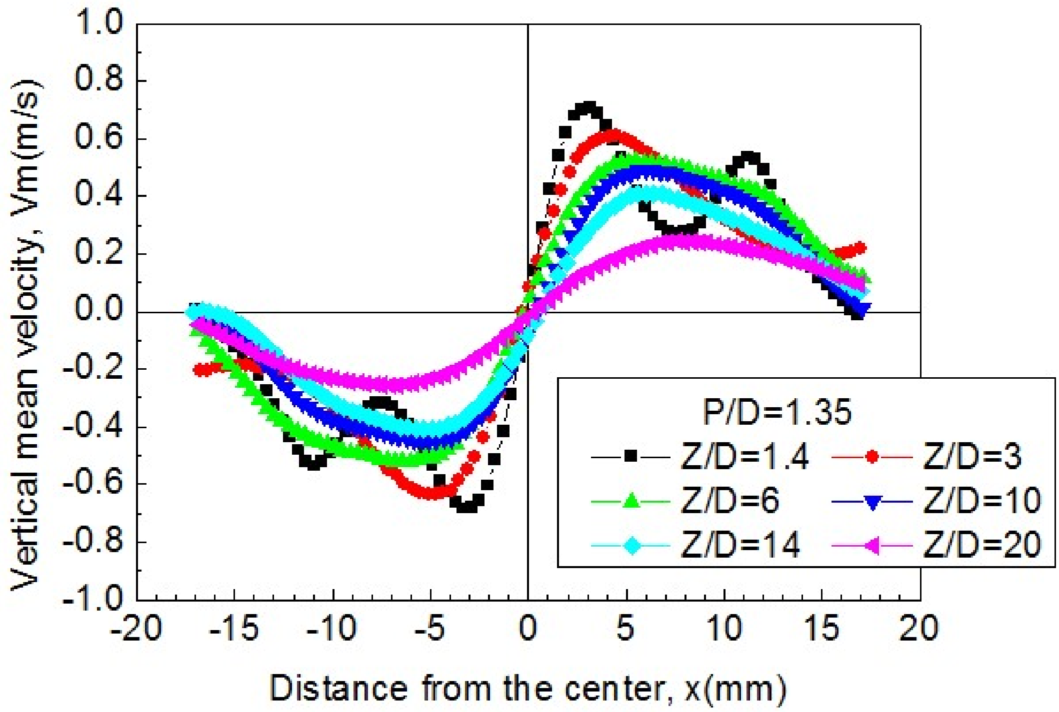

FIG. 16. Mean vertical velocity profiles in the central subchannel for regular bundle (P/D = 1.35).

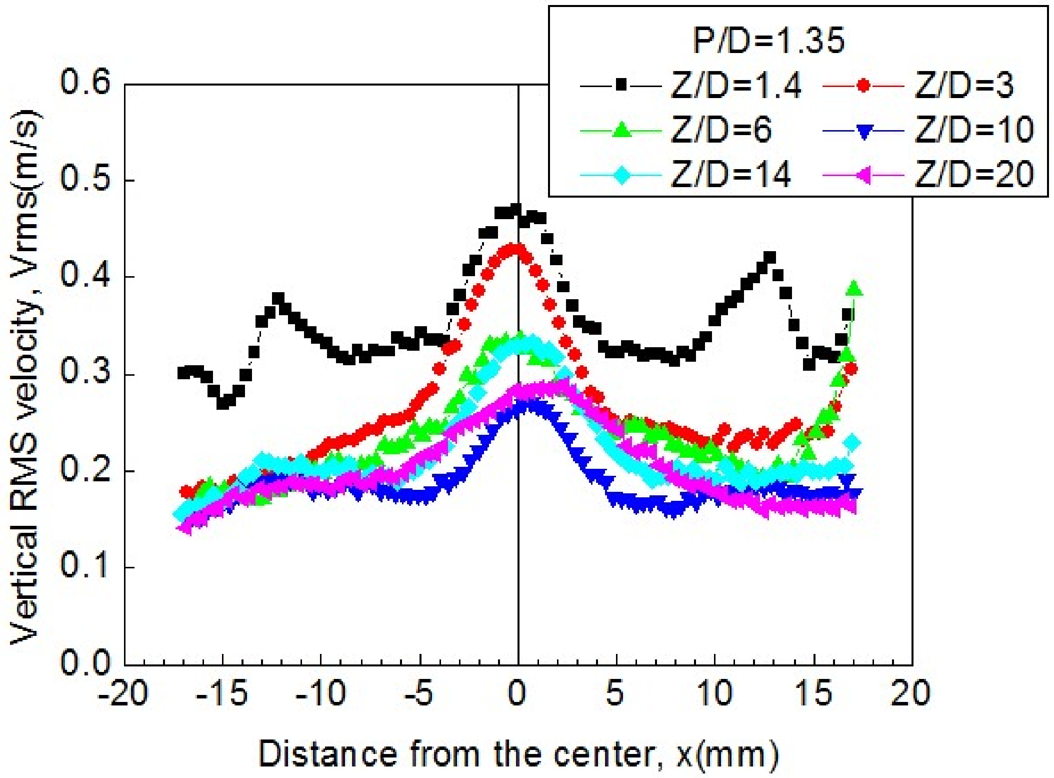

FIG. 17. RMS vertical velocity profiles in the central subchannel for regular bundle (P/D = 1.35).

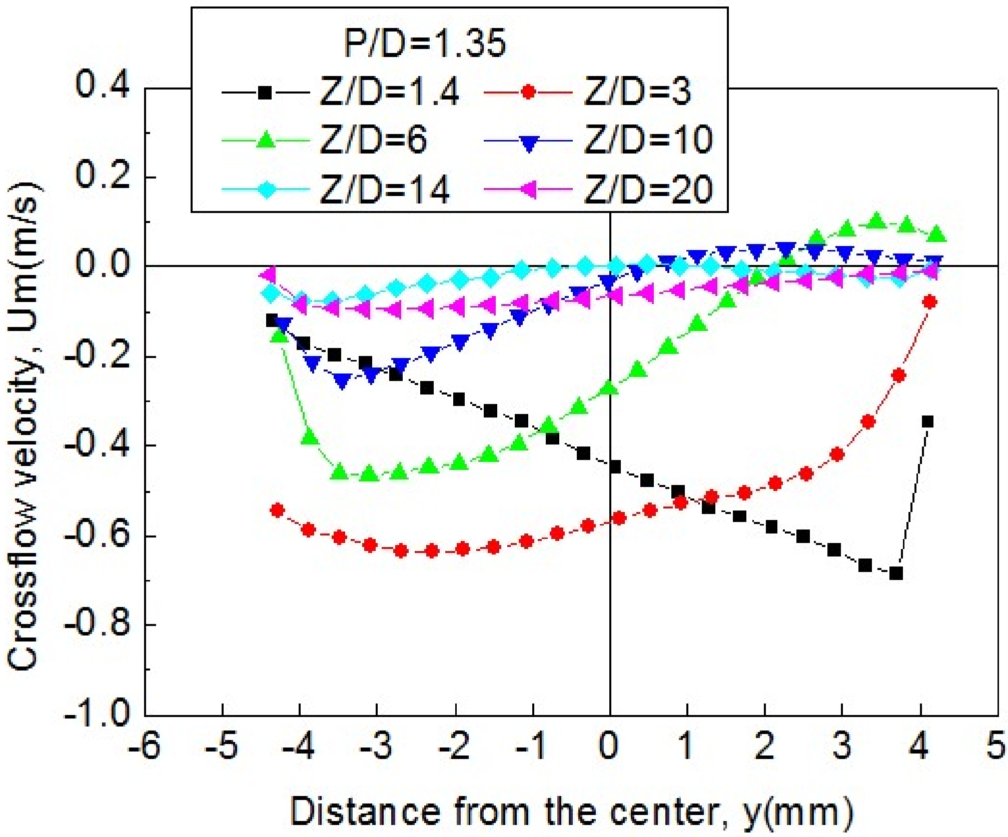

FIG. 18. Crossflow velocity profiles in the left gap of central subchannel for regular bundle (P/D = 1.35).

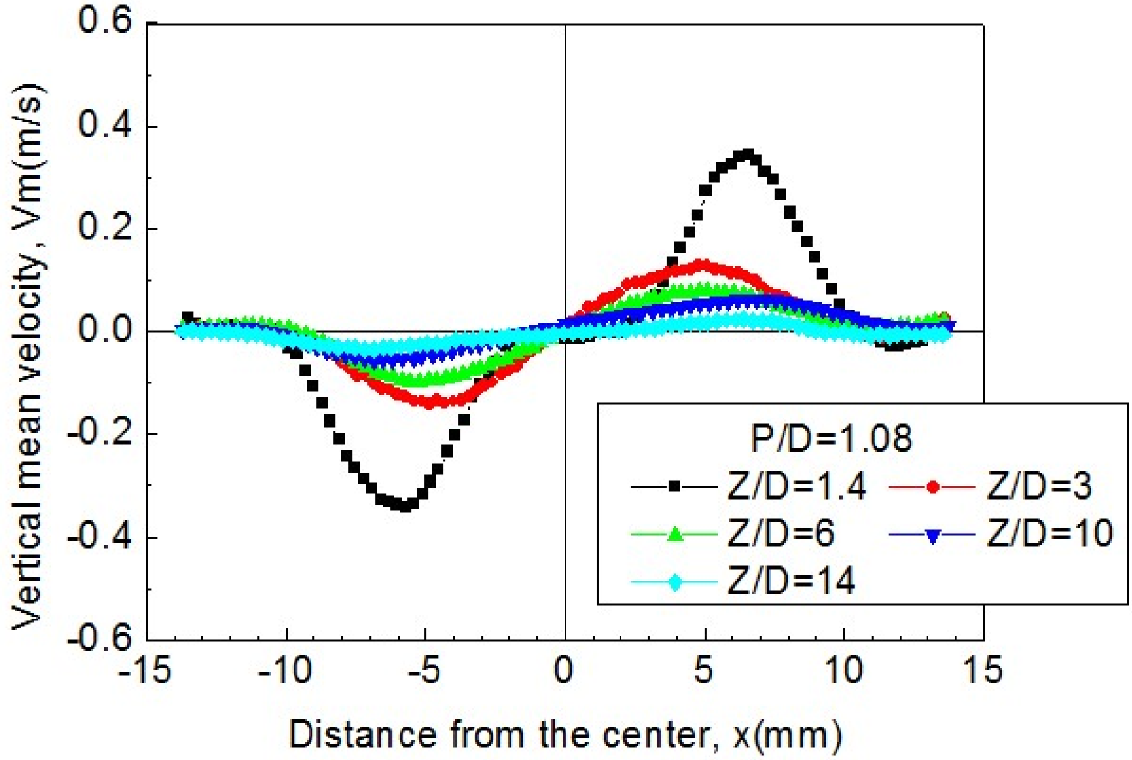

FIG. 19. Mean vertical velocity profiles in the central subchannel for tight lattice bundle (P/D = 1.08).

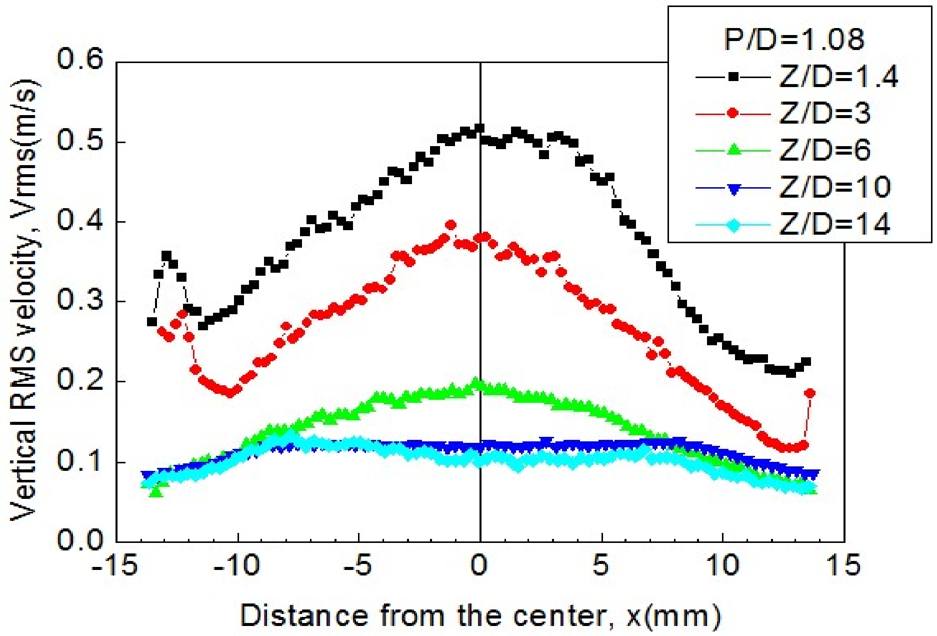

FIG. 20. RMS vertical velocity profiles in the central subchannel for tight lattice bundle (P/D = 1.08).

The measurement error for axial and lateral velocity is estimated by combining the systematic and random error sources. The PIV measurement error for lateral velocity includes the calibration error and image mismatching error as primary error components. Total measurement error of mean lateral velocity is calculated by root–sum–square technique for the calibration error and image mismatching error. The measurement error of mean lateral velocity is estimated to 5.9 % and 9.1 % for regular bundle (P/D = 1.35) and tight lattice bundle (P/D = 1.08), respectively. The LDV measurement error for axial velocity includes the systematic error (3.5 %) and the random error (1 % for mean velocity, 1.8 % for RMS velocity). Total measurement error for axial velocity is estimated to 7.3 % and 8.2 % for the mean velocity and the RMS velocity, respectively. The measurement error is listed in Table 2.

TABLE 2. SUMMARY OF MEASUREMENT ERROR IN AXIAL AND LATERAL VELOCITIES

P/D	Axial mean velocity(Wm)	Axial RMS velocity(Wrms)	Lateral mean velocity(Vm)
1.08	7.3 %	8.2 %	5.9 %
1.35	7.3 %	8.2 %	9.1 %

2.3. HEAT–TRANSFER EXPERIMENT

A heat transfer experiment was carried out in the flow mixing test loop, OFEL, in order to measure the rod wall temperature for regular and tight lattice bundles. The test section consists of 4x4 rod bundle with single heated rod in one of the four central rod positions. Figure 21 shows the schematic of test section with a heated rod, rod support grid and twist–vane grid. It indicates the initial elevation of the thermocouples in the test bundle just upstream of the twist–vane spacer grid (z/D = –2.6). To measure the temperature distribution around the heated rod downstream of the spacer grid, the heated rod assembly was simply moved upwards along in axis and then fixed at the target axial locations (i.e. z/D = 1.5, 2.0, 2.5, 3.0, 5.0, 10.0 and 12.0). Then, the temperature measurements were taken.

The design of the heated section is shown in more detail in Fig. 22. One 90° quadrant of the heated, stainless steel tube section had five slots machined into it around the circumference to accommodate thermocouples for measuring the rod wall surface temperature. These slots were machined very precisely, and each is 1 mm in width, 1 mm in depth, and 5 mm in length. T–type thermocouples of diameter 1 mm were welded carefully into these slots, and their lead wires pulled out through the gap between the steel/copper tubes and the central copper rod, the rod and tubes electrically insulated from each other by the Teflon sleeve. Figure 23 shows the cross–sectional view of the five thermocouple positions in the heated rod to measure the rod wall temperature distribution over the 90 degree quadrant of the heater surface.

The experimental conditions for this thermal bundle test are summarized as follows.

- Bundle flow velocity: 1.5 m/sec
- Heat flux (outer surface): 104 kW/m2
- Number of samples taken to obtain averaged temperature data: 150
- (The time interval between measurements is 1 second)
- The inlet temperatures (measured at the inlet of the test section) vary from 11 ºC to 14 ºC, depending on the axial position of the heated section.

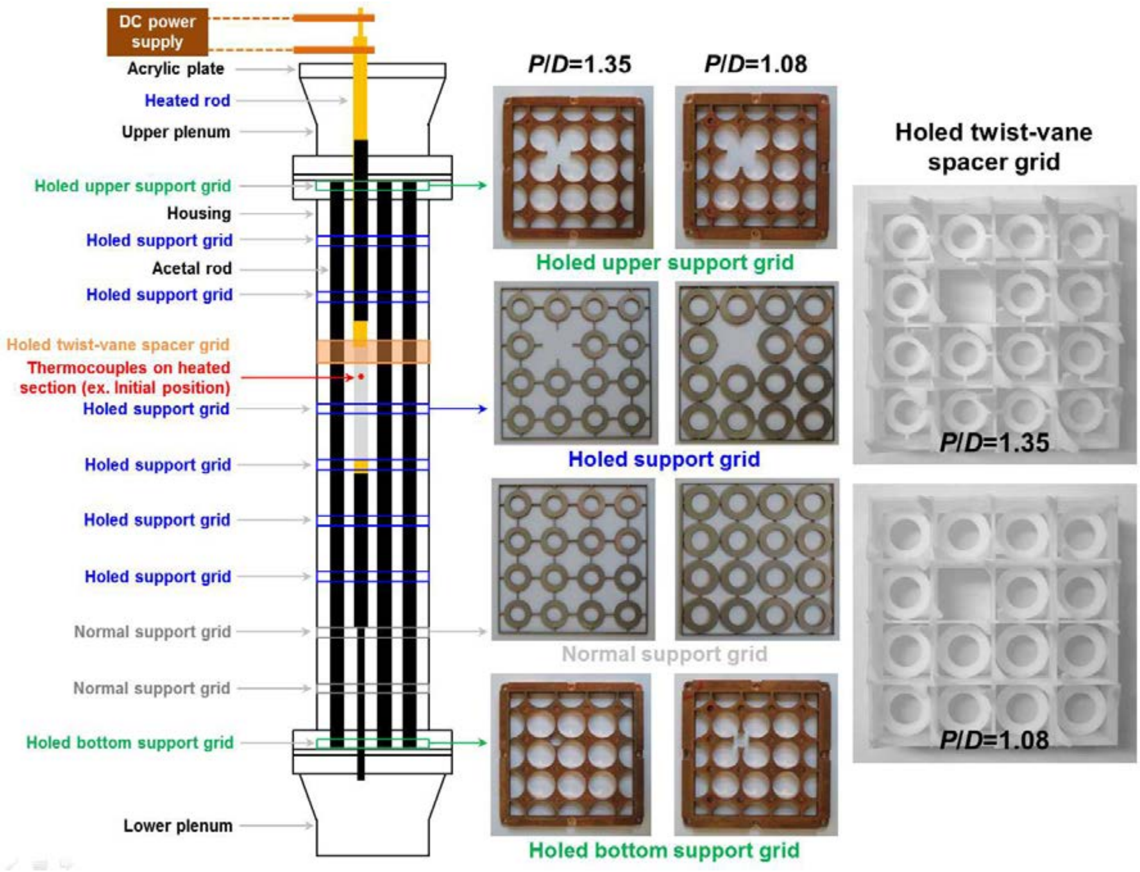

FIG. 21. Schematic of heated test section, rod support grid and twist–vane grid (Reproduced courtesy of KAERI [8]).

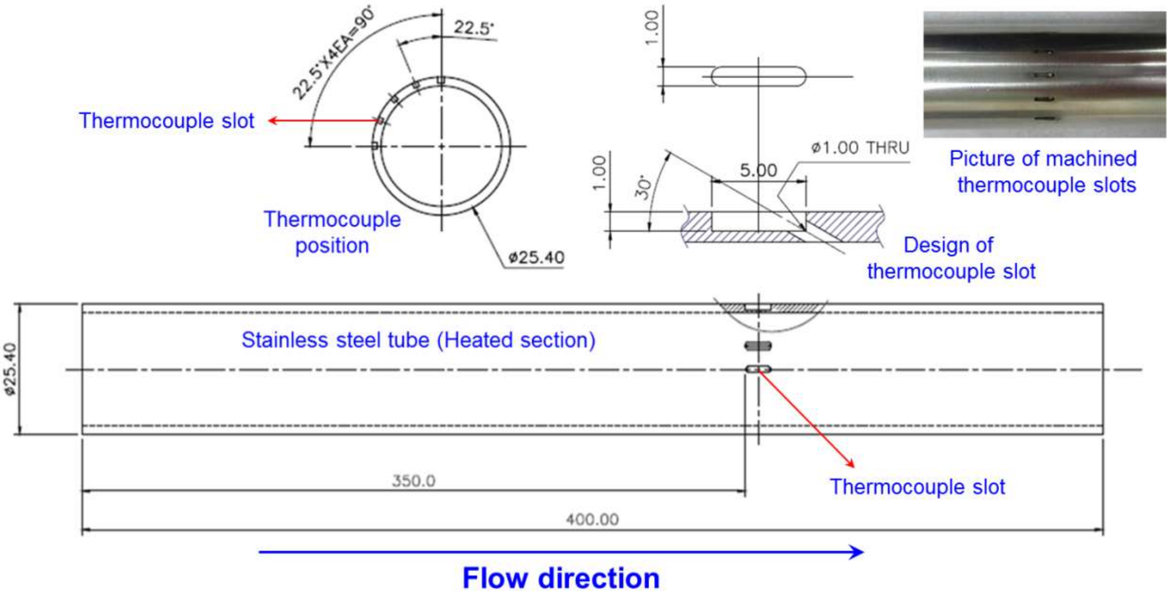

FIG. 22. Design of heated section with five thermocouples (Reproduced courtesy of KAERI [8]).

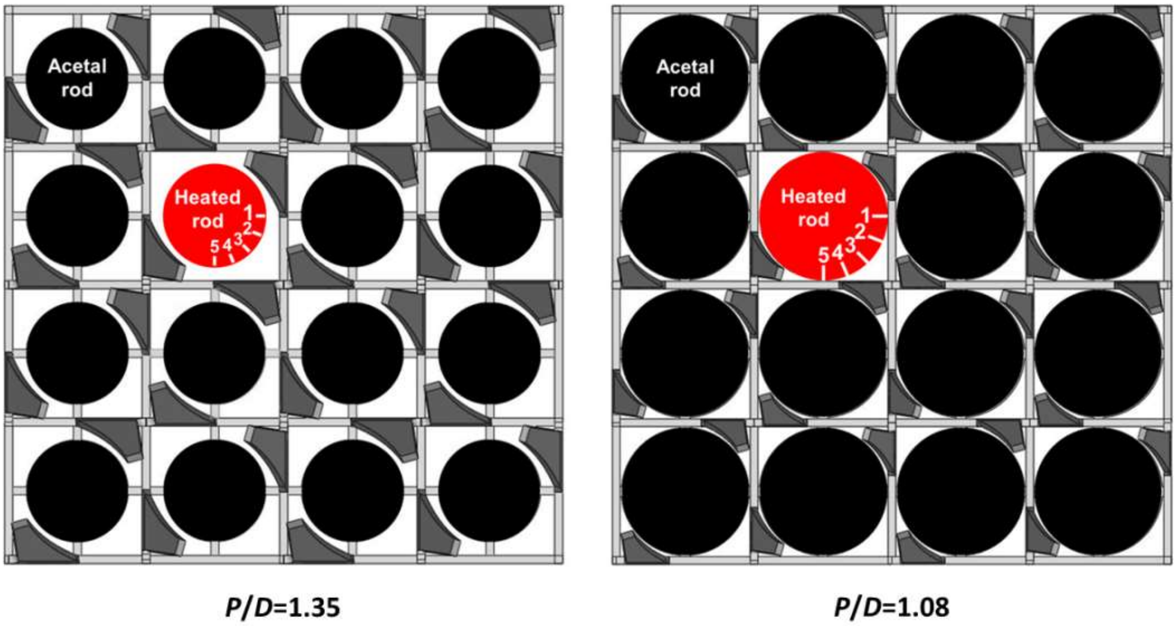

FIG. 23. Cross–sectional view of the five thermocouples for regular and tight lattice bundles (Reproduced courtesy of KAERI [8]).

Figure 24 shows the circumferential variation of rod temperature at various axial locations for regular bundle (P/D = 1.35). The temperature variation is 2 ºC and 3 ºC at the near downstream locations (z/D < 5) and far downstream location (z/D = 10), respectively. The rod temperature at position 2 (DTw2) is minimum that indicates higher heat transfer due to a deflecting flow directed to this position by the twist vane. Figure 25 shows the axial variation of rod temperature downstream of the twist–vane grid. The rod temperature decreases near downstream of the twist vane (z/D = 2–3) and increases farther downstream. This result means the heat transfer enhancement by the twist vane. The heat transfer increases by 30 % (maximum) for the position 2 and 15 % (minimum) for the positions 4 and 5 (DTw4 & DTw5).

Figure 26 shows the circumferential variation of rod temperature at various axial locations for tight lattice bundle (P/D = 1.08). The temperature variation is 3 ºC and 2 ºC at the near downstream location (z/D = 1.5) and further downstream locations (z/D > 10), respectively. The rod temperature at position 2 (DTw2) is minimum that indicates higher heat transfer due to a deflected flow by the twist vane. Figure 25 shows the axial variation of rod temperature downstream of the twist–vane grid. The rod temperature is minimum near downstream of the twist vane (z/D = 1.5) and increases farther downstream. This result means the heat transfer enhancement by the twist vane. The heat transfer increases by 43 % (maximum) for the position 2 and 28 % (minimum) for the positions 4 and 5 (DTw4 & DTw5). It is noted that the heat transfer enhancement in tight lattice bundle is higher than the regular–bundle result.

The measurement error of rod temperature is estimated by combining random and systematic errors using root–sum–square technique. The bounding random error is calculated to be 0.2 ºC from the standard deviation of measured temperature. The systematic error is evaluated from the accuracy in thermocouple and data acquisition (DAQ) system. The T–type thermocouple accuracy is 0.3 ºC and the DAQ accuracy (Agilent) is 0.6 ºC. Hence, total error of temperature measurement is bounded by 1.4 ºC. The measured rod temperature and error are provided in detail to the participants.

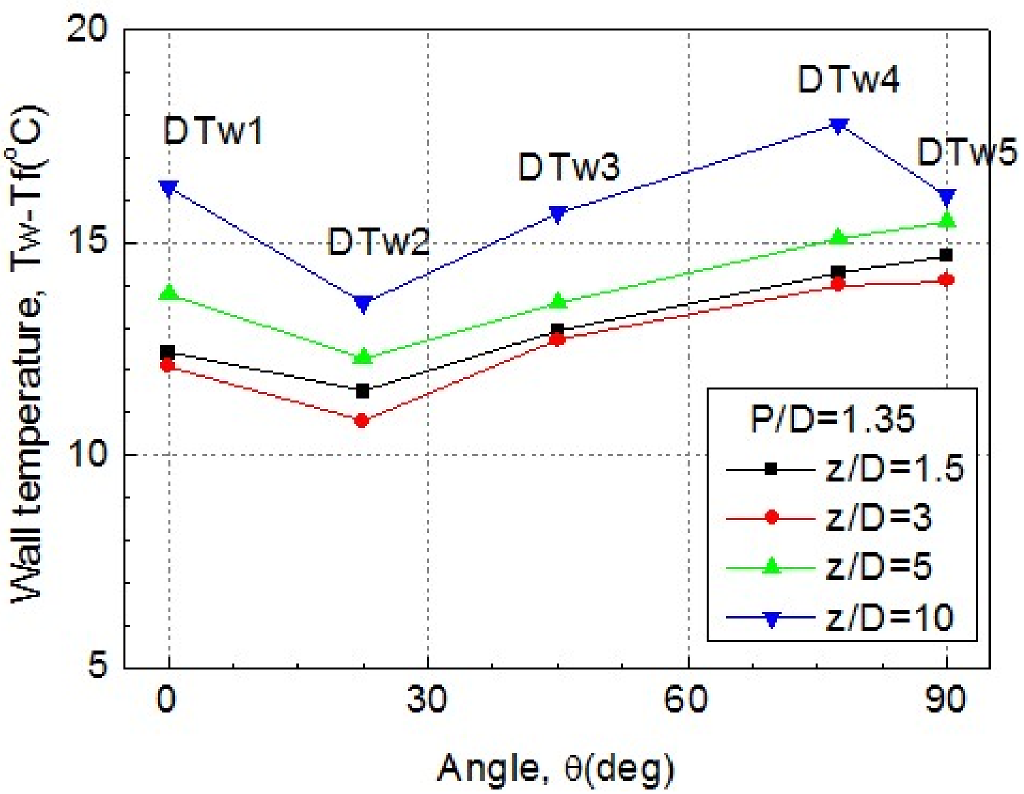

FIG. 24. Circumferential variation of rod temperature in regular bundle (P/D = 1.35).

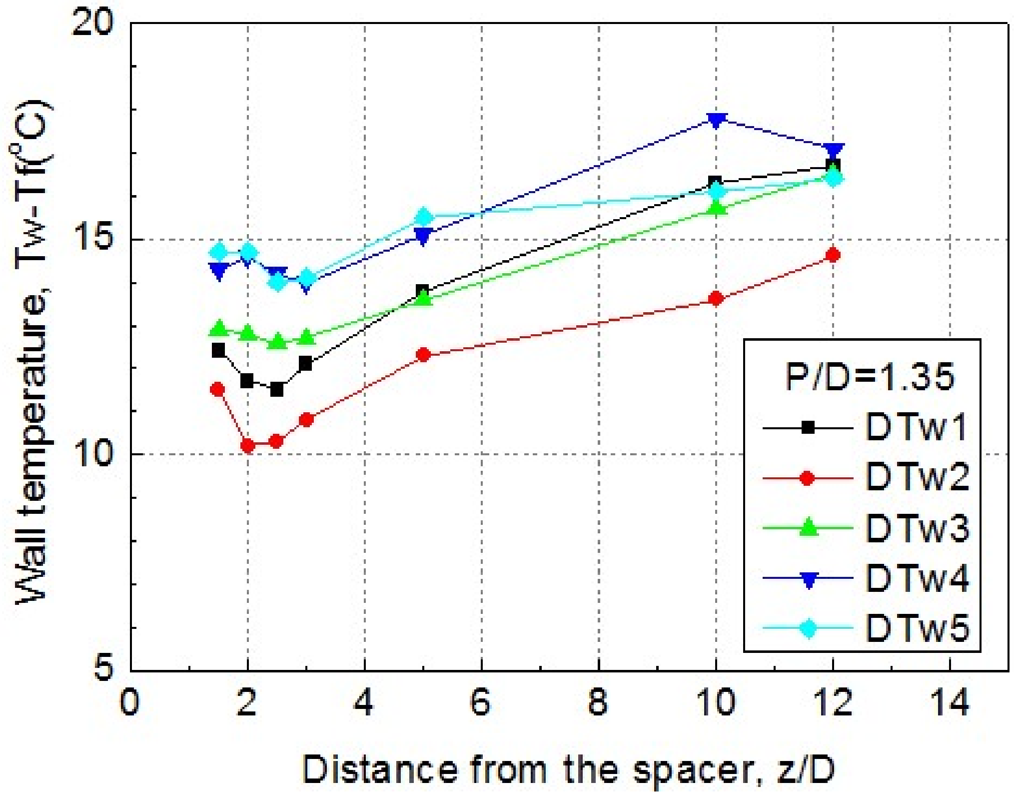

FIG. 25. Axial variation of rod temperature in regular bundle (P/D = 1.35).

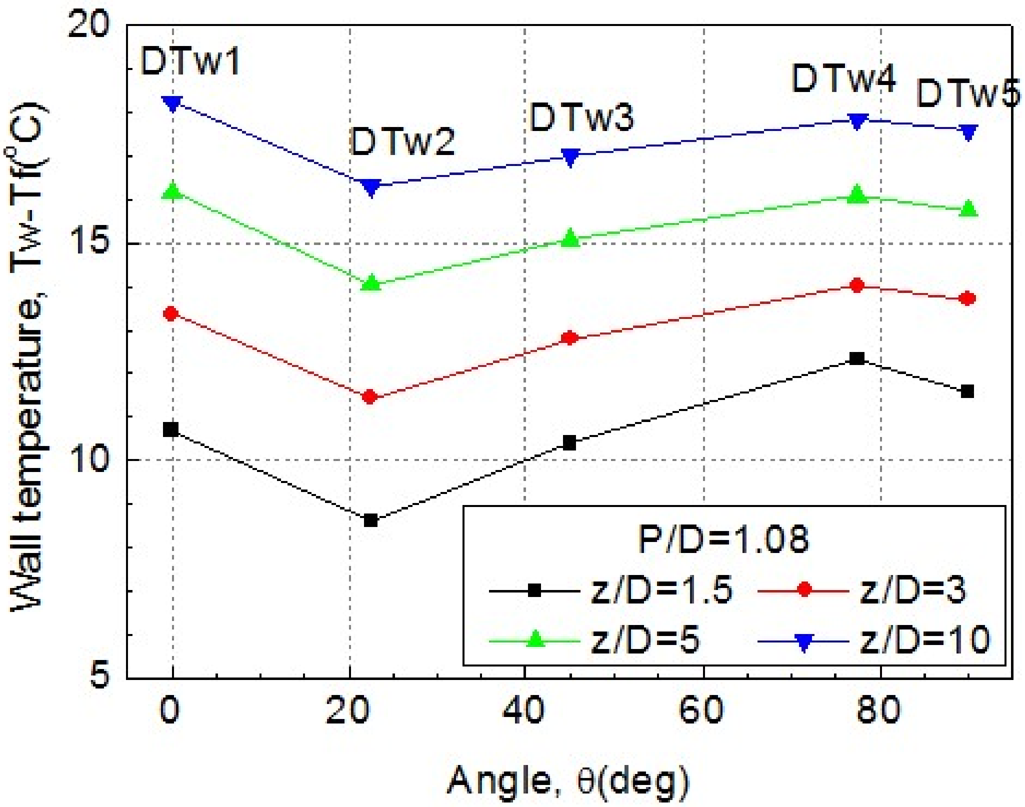

FIG. 26. Circumferential variation of rod temperature in tight lattice bundle (P/D = 1.08.)

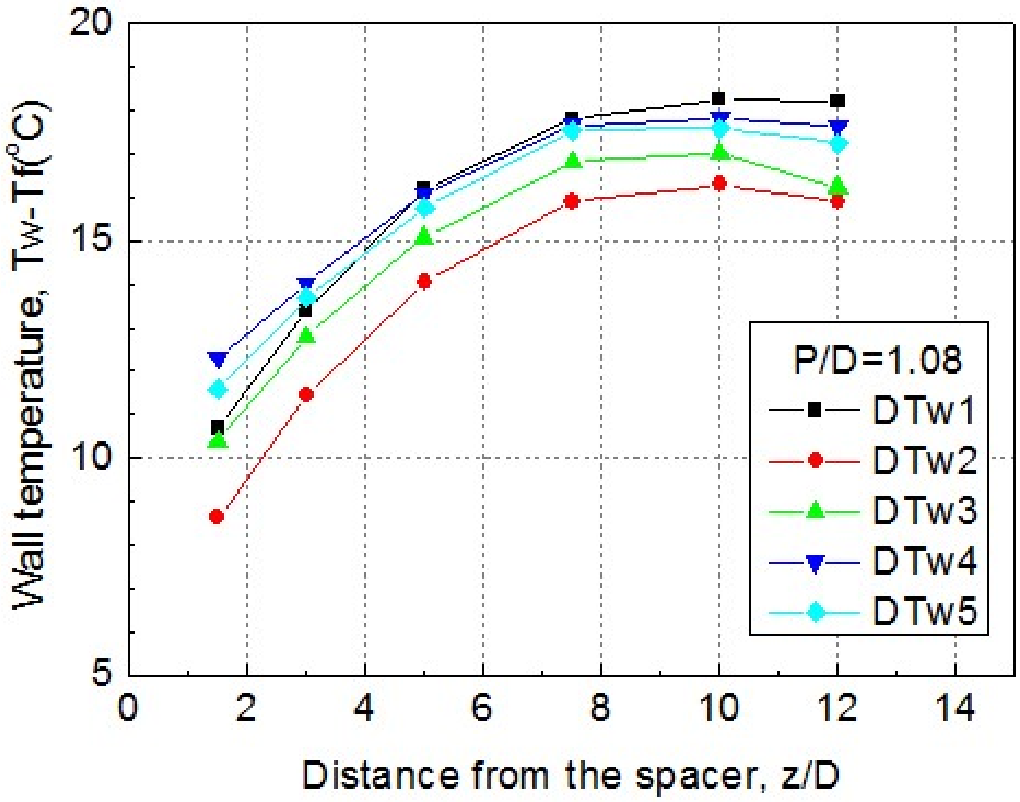

FIG. 27. Axial variation of rod temperature in tight lattice bundle (P/D = 1.08).

3. STATISTICS OF KAERI BUNDLE BENCHMARKS

3.1. PARTICIPANTS AND CODES USED

Twelve organizations from nine countries have participated in this IAEA CRP and are listed in Table 3. Seven organizations submitted the CFD results for the isothermal and thermal KAERI bundle tests. Table 4 shows the summary status of organization participating in the KAERI bundle benchmark. BARC from India, KAERI from Republic of Korea and VNIIAES from the Russian Federation submitted the CFD results for all isothermal and thermal tests with regular bundle (P/D = 1.35) and tight lattice bundle (P/D = 1.08). CEA from France and SJTU from China provided the CFD results for isothermal test with regular bundle (P/D = 1.35). CNL from Canada submitted the CFD result for thermal test with tight lattice bundle (P/D = 1.08). NPIC from China submitted the CFD result for isothermal test with regular bundle (P/D = 1.35).

TABLE 3. LIST OF CRP PARTICIPANTS

Country	**Organization**	**CRP Participant**
Algeria	CRNB	Mr. Y. Bouaichaoui
Canada	CNL	Mr. K. Podila
China	SJTU	Mr. J. Xiong
China	NPIC	Mr. Z. Li
France	CEA	Mr. U. Bieder
Germany	HZDR	Mr. T. Hoehne
India	BARC	Mr. N. K. Maheshwari
Republic of Korea	KAERI	Mr. W. K. In
Switzerland	Goldsmith Transactions	Mr. B. L. Smith
Switzerland	PSI	Mr. B. Niceno
Russian Federation	VNIIAES	Mr. M. Starodubtsev
Russian Federation	OKB GIDROPRESS	Mr. A. Skibin

TABLE 4. PARTICIPATION IN KAERI BUNDLE BENCHMARK

Test Category	P/D	Organization provided results (Y = yes)						
		BARC	CEA	CNL	KAERI	NPIC	SJTU	VNIIAES
Isothermal	1.08	Y			Y	Y		Y
	1.35	Y	Y		Y	Y	Y	Y
Heated	1.08	Y		Y	Y			Y
	1.35	Y	Y		Y		Y	Y

3.2. SUMMARY OF CFD METHOD

Table 5 summarizes the CFD methods adopted by the different organizations for the KAERI bundle benchmark. Five organizations (CNL, KAERI, NPIC, SJTU, VNIIAES) used commercially available CFD software (STAR–CCM+, CFX). BARC used the open source software, OpenFOAM, while CEA used the in–house developed software, TrioCFD. Six of the participating organizations adopted RANS–based turbulence models, while CEA performed the CFD analysis with large eddy simulation (LES) as well as non–linear k–εpsilon RANS model. For the inlet boundary condition, two organizations (BARC and CEA) applied a fully–developed flow and five organizations (CNL, KAERI, NPIC, SJTU, VNIIAES) applied a uniform flow. All seven organizations used a constant pressure at the outlet boundary. Four organizations (BARC, CEA, SJTU, VNIIAES) used a constant heat flux at the inner surface of heated rod (clad) and two organizations (CNL, KAERI) applied a constant heat source in heated rod. The mesh types are tetrahedral, polyhedral and hybrid cells. The total number of mesh cells varied from 8 million (min.) and 320 million (max.). The non–dimensional distance to the first cell from wall boundary (y+w) varies from 0.004 (CNL) to 52 (KAERI) according to the requirement of the near wall treatment adopted. The CFD methods used by the seven organizations are summarized in Table 5 and described in detail below.

TABLE 5. SUMMARY OF CFD METHOD FOR THE KAERI BUNDLE BENCHMARK

	BARC	**CEA**	**CNL**	**KAERI**	**NPIC**	**SJTU**	**VNIIAES**
CFD code	OpenFOAM	TrioCFD	CCM=9.0	CFX18.0 CCM+11	CCM+10	CCM+10	CCM+11
Turb. model	SST	NL k-e	SST	RNG, SST Realizable	Realizable	k-e Realizable	RSM
Inlet B.C.	fully dev.	fully dev.	uniform	uniform	uniform	uniform	uniform
Outlet B.C.	const. P	const. P	const. P	const. P	const. P	const. P	uniform
Mesh type	hybrid	tetra	ply	tetra / poly	tetra / poly	hexa-dominant	poly
# cells	8-20M	20-320M	23-60M	53-73M	115-159M	112-134M	182-280M
y^+@ z/D = 10	1.4-1.6	4-25	0.004-4	26-52	7-17	15-50	0.1-1

<u>BARC</u>

CFD codes: OpenFOAM 2.2.2 for P/D = 1.35 and OpenFOAM 4.1 for P/D = 1.08
Turbulence model: SST k–w
Advection scheme: 2nd order UPWIND
Computational domain:

— Lateral direction: 4x4 rod bundle
— Axial direction: 1 m (Z/D = –21D, 21D)
— Heated rod: single rod (heated length = 400 mm)

Boundary conditions:

- Inlet: mapped velocity from bare rod simulation having average inlet velocity of 1.5 m/s & uniform temperature
- Outlet: constant pressure
- Heated wall: constant heat flux 115.15 kW/m2 @inner surface of heated tube

Meshing Parameter:

Test	P/D	Mesh type	Number of cells	Number of prism layers	y+w @ z/D = 10
Isothermal test	1.35	Hybrid (Tetra, Hexa, Prism and Pyramid)	8.5M–13M	3	8–16 (13M)
	1.08	Hybrid	20M	2	1.4–6.8
Heated–rod test	1.35	Hybrid	8.5M	3	4–10
	1.08	Hybrid	21M	2	2.3–6.14

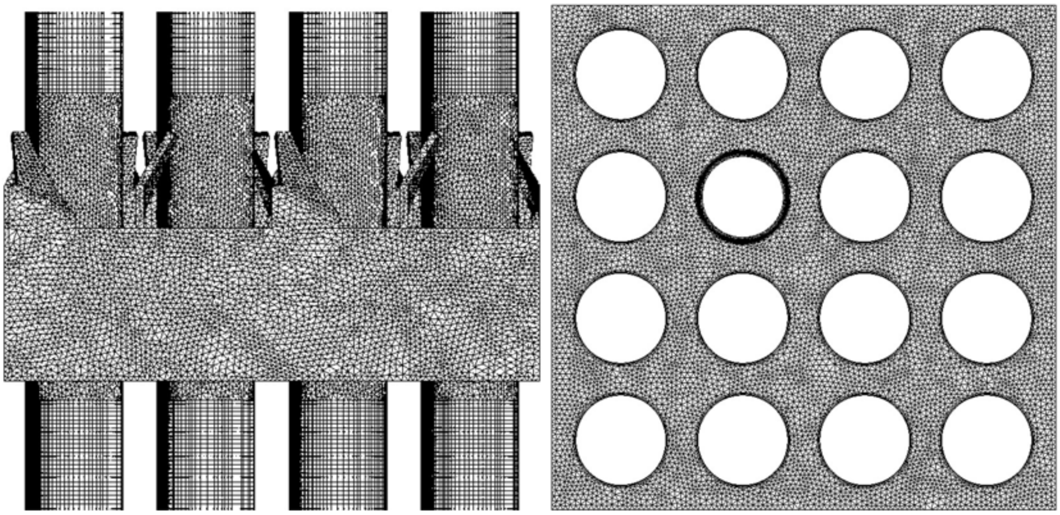

FIG. 28. Hybrid mesh for OpenFOAM (8.5M, P/D = 1.35).

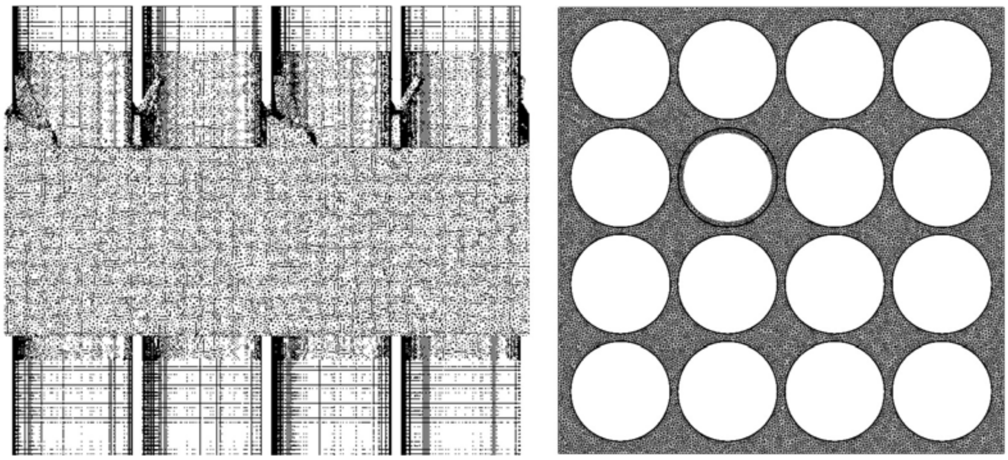

FIG. 29. Hybrid mesh for OpenFOAM (21M, P/D = 1.08).

CEA

CFD codes: TrioCFD
Turbulence model: LES, k–εpsilon based non–linear eddy viscosity model
Advection scheme: 2nd order centred & 2nd order TVD
Computational domain:

- Lateral direction: 4x4 rod bundle
- Axial direction: 1.6 m (Z/D = –16.6D, 24D)
- Heated rod: single rod (heated length = 400 mm)

Boundary conditions:

- Inlet: uniform for T; fully developed profiles for u, k, eps
- Outlet: constant pressure
- Heated wall: constant heat flux 115.15 kW/m2 @inner surface of heated tube

Meshing parameter:

Test	P/D	Mesh type	Number of cells	Number of prism layers	y+w @ z/D = 10
Isothermal test	1.35	Tetrahedron	20 M 40 M 320 M	2 2 4	25 10 4
Heated–rod test	1.35	Tetrahedron	20 M 20 M 40 M	1 2 2	30 30 15

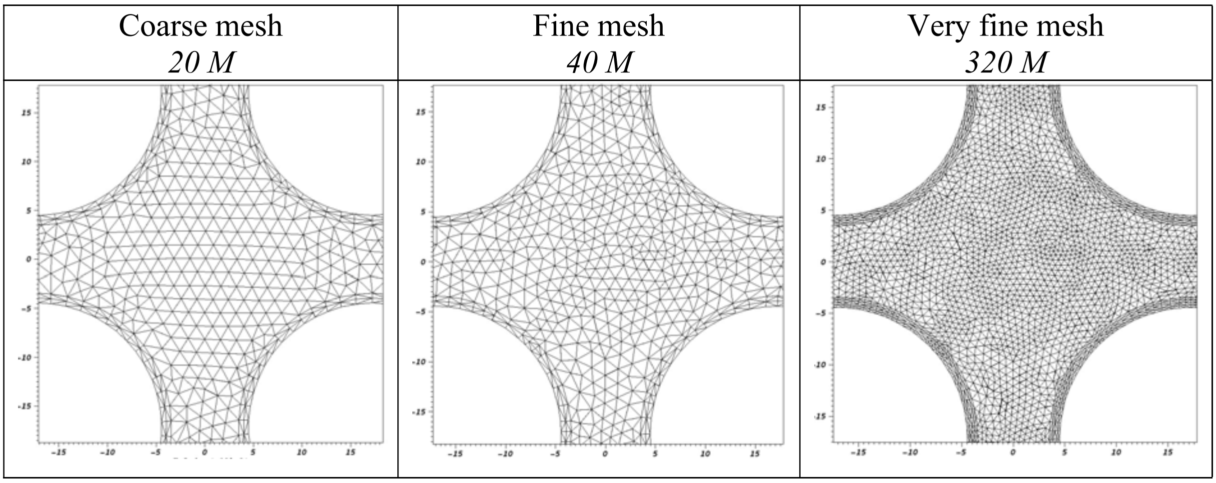

FIG. 30. Mesh for isothermal test

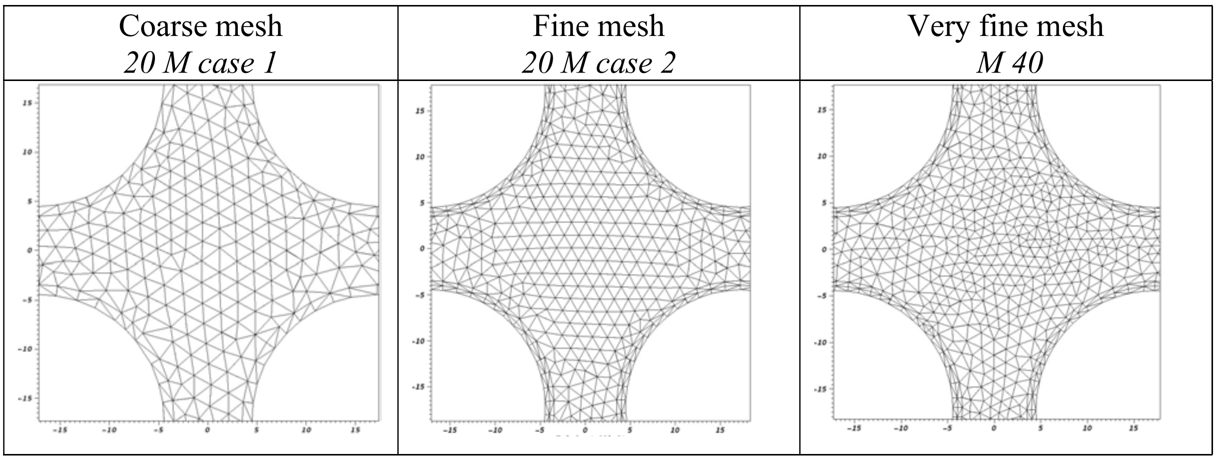

FIG. 31. Mesh for thermal test.

CNL

CFD codes: STAR–CCM+ 9.0

- Turbulence model: SST k–□

Advection scheme:

- Second–order upwind for flow, and energy
- First–order upwind for turbulence

Computational domain (Fig. 3.5):

- Lateral direction: 4x4 rod bundle
- Axial direction: 2 m
- Heated rod: single rod (heated length = 400 mm)

Boundary conditions:

- Inlet: uniform velocity & temperature
- Outlet: constant pressure
- Heated wall: constant heat source (Conjugate Heat Transfer)

Meshing parameters:

Test	P/D	Mesh type	Number of cells	# of cells within a prism layer	y+
Heated	1.08	Polyhedron	23M–60M tested, 23M used for submission (Obtained through mesh sensitivity)	5	$0.01\leq y^{+}_{grid} \leq 0.78$ $0.004\leq y^{+}_{rods}\geq 4$ $0.003\leq y^{+}_{vane} \leq 5$

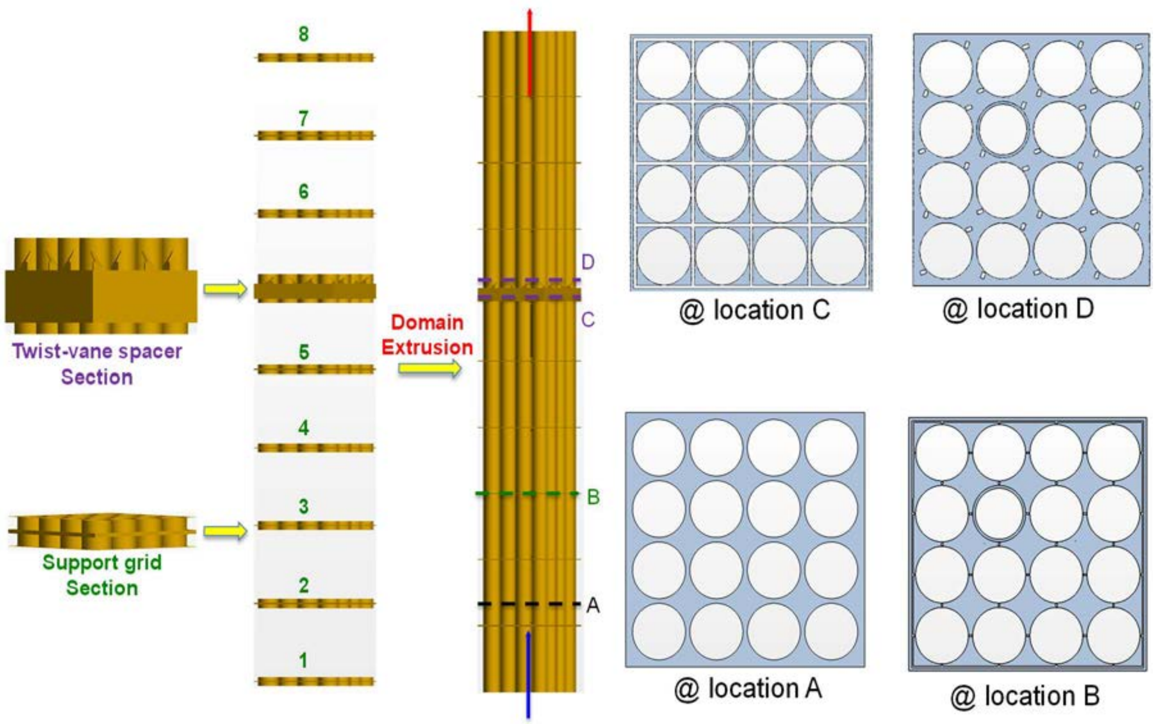

FIG. 32. Computational domain development for the 4×4 rod bundle assembly with eight support grids and a twisted–vane spacer.

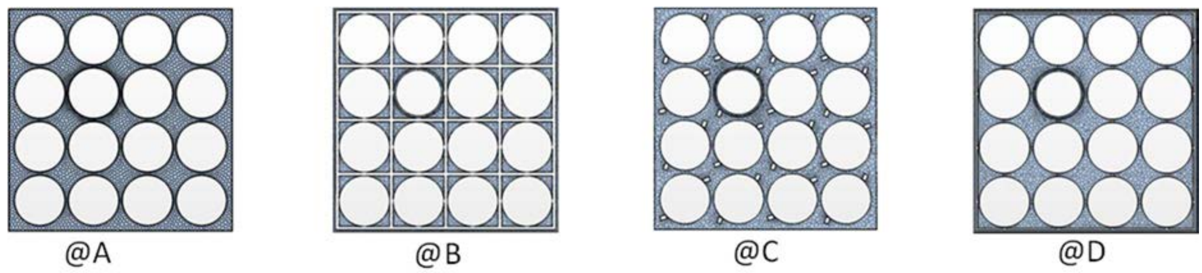

FIG. 33. Snap shot of the cross sectional meshes.

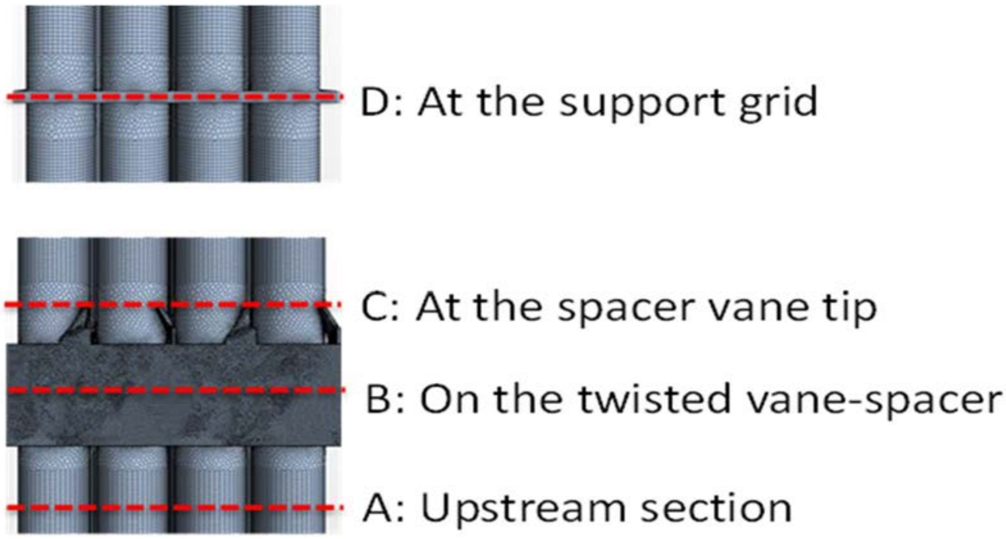

FIG. 34. Mesh on the support grid and the vane spacer.

KAERI

CFD codes: CFX 18.0, STAR–CCM+ 11.0
Turbulence model:
- CFX: k–ε, RNG k–ε, SST k–w
- STAR–CCM+: k–ε, Realizable, SST k–w

Advection scheme:
- CFX: High resolution (Hybrid scheme of 1st and 2nd – order Upwind)
- STAR–CCM+: 2nd order Upwind

Computational domain:
- Lateral direction: 4x4 rod bundle
- Axial direction: 3 m (Z/D = –40D, 80D)
- Heated rod: single rod (heated length = 3 m, assumed full–length heating)

Boundary conditions:
- Inlet: uniform velocity & temperature
- Outlet: constant pressure
- Heated wall: constant heat source

Meshing parameters:

Test	P/D	Mesh type	Number of cells	Number of prism layers	y^+_w @ z/D = 10
Isothermal test	1.35	Tetrahedral	64M	3	28–52
		Polyhedral	73M	3	5–8
	1.08	Tetrahedral	82M	3	26–50
		Polyhedral	46M	3	5–8
Heated–rod test	1.35	Tetrahedral	43M	3	27–52
		Polyhedral	67M	3	14–24
	1.08	Tetrahedral	117M, 150M	3	13–23 (0.8–2.8 150M_SST)
		Polyhedral	100M–120M	3	1.5–10

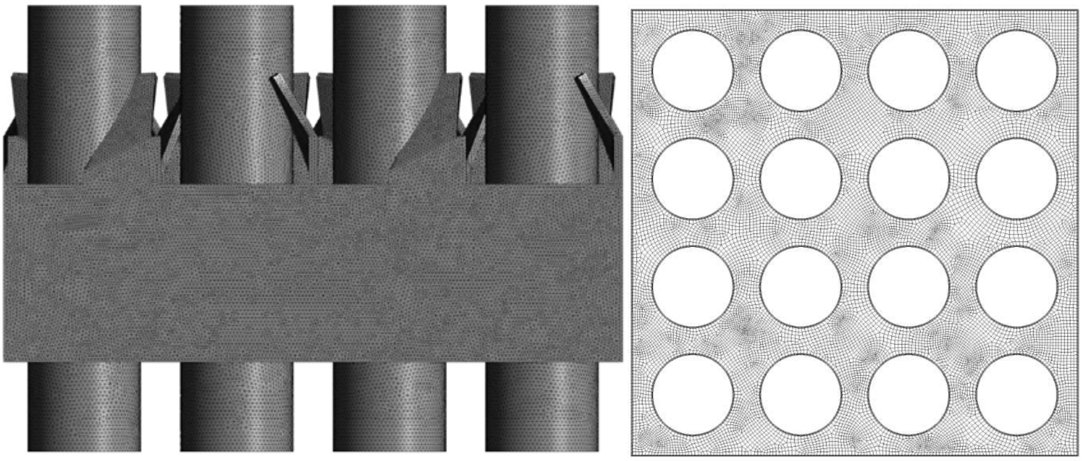

FIG. 35. Tetrahedral mesh for CFX (64M, P/D = 1.35).

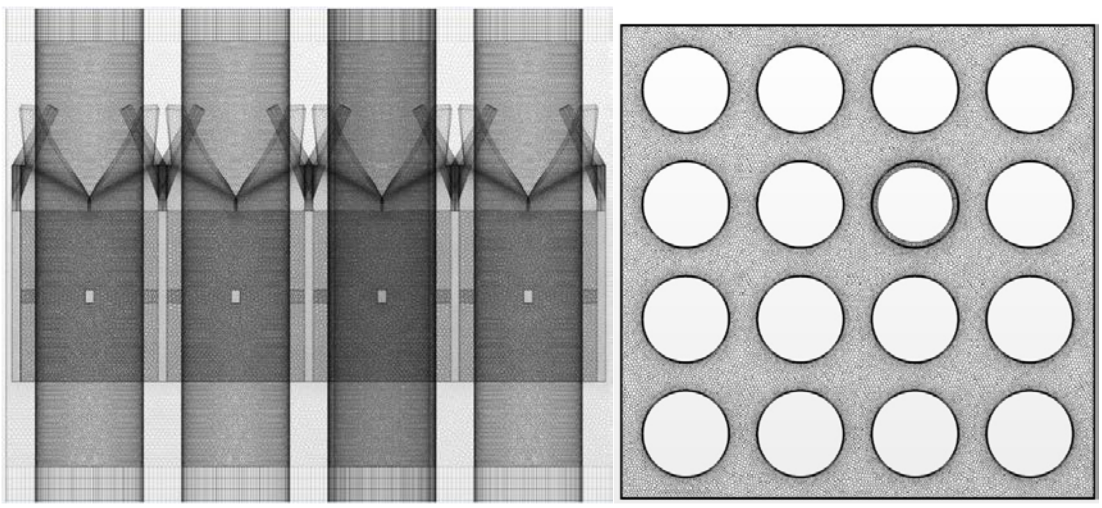

FIG. 36. Polyhedral mesh for STAR–CCM+ (67M, P/D = 1.35).

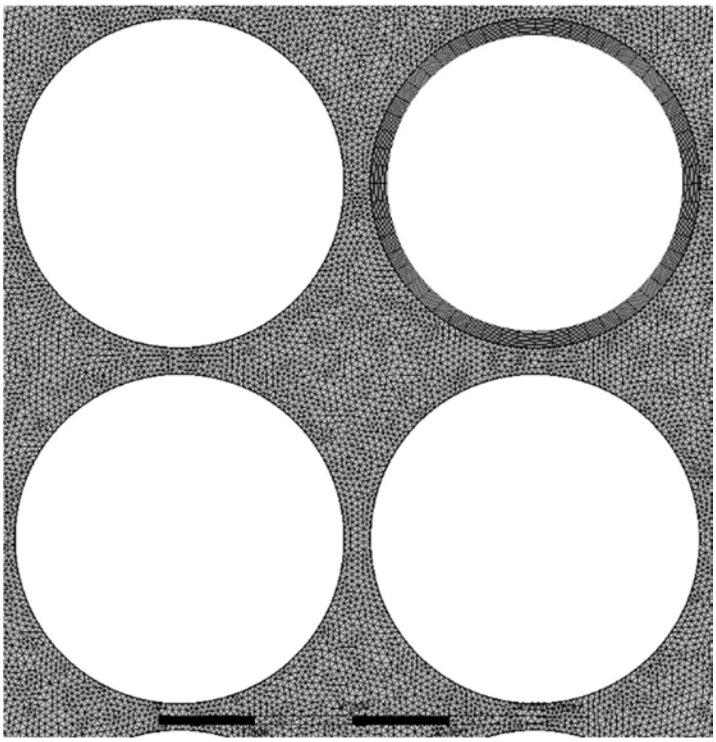

FIG. 37. Tetrahedral mesh for CFX (150M, P/D = 1.08).

<u>NPIC</u>

CFD codes: STAR–CCM+ 10.02
Turbulence model: Realizable k–ε two‑layers
Advection scheme: 2nd order UPWIND
Computational domain:

— Lateral direction: 4x4 rod bundle
— Axial direction: 1 m (Z/D = –10D, 20D)
— Heated rod: not applicable

Boundary conditions:

— Inlet: uniform velocity(average axial velocity = 1.5m/s)
— Outlet: constant pressure
— Heated wall: not applicable

Meshing parameters:

Test	P/D	Mesh type	Number of cells	Number of prism layers	y^+_w @ z/D = 10
Isothermal test	1.35	Tetrahedron	115M	3	10 ‑ 17
	1.08	Tetrahedron	159M	3	7 ‑ 9

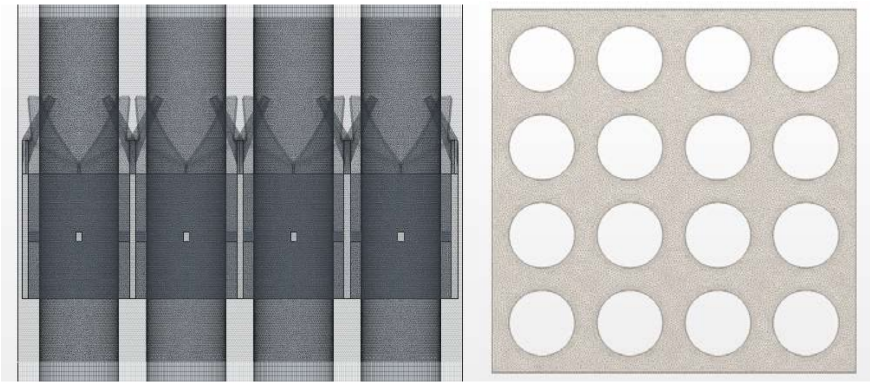

FIG. 38. Tetrahedral mesh for CFX (115M, P/D = 1.35).

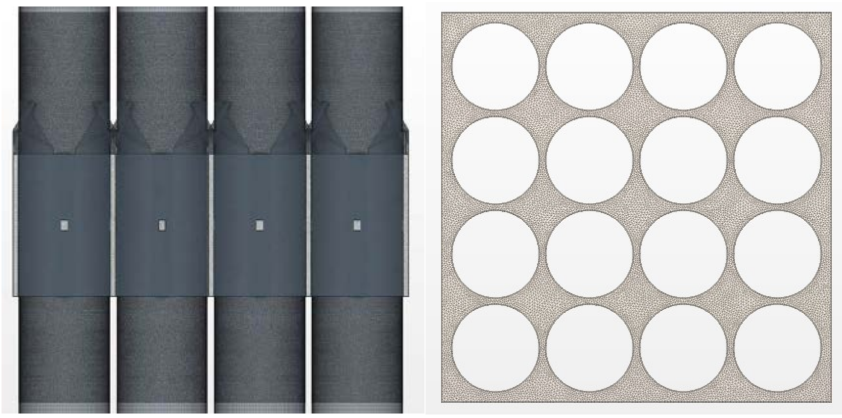

FIG. 39. Polyhedral mesh for STAR–CCM+ (159M, P/D = 1.08).

SJTU

CFD codes: STAR–CCM+ 10.02
Turbulence model: Realizable k–εpsilon
Advection scheme: Second order Upwind
Computational domain:

- Lateral direction: 4x4 rod bundle
- Axial direction: 2 m (Z/D = –27D, 53D)
- Heated rod: single rod (heated length = 2 m)

Boundary conditions:

- Inlet: uniform velocity & temperature
- Outlet: constant pressure
- Heated wall: constant heat flux @inner surface

Meshing parameters:

Test	P/D	Mesh type	Number of cells	Number of prism layers	y^+_w @ z/D = 10
Isothermal test	1.35	Polyhedron	134M	3	28–50
Heated–rod test	1.35	Hexa–dominant (Trimmed)	112M	3	15–30

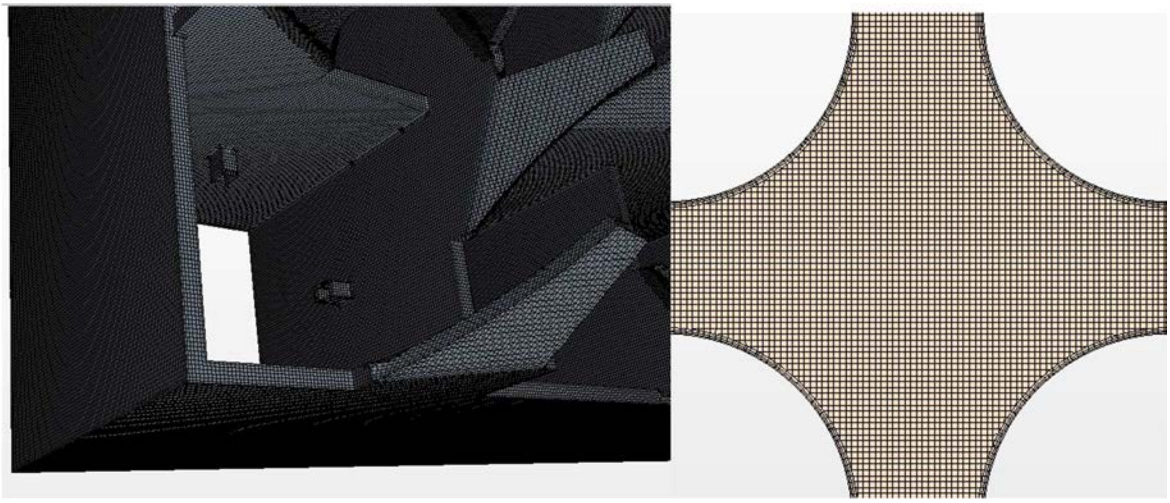

FIG. 40. Hexa–dominant (Trimmed) mesh for STAR–CCM+ (134M, P/D = 1.35)

<u>VNIIAES</u>

CFD codes: STAR–CCM+ 11.0
Turbulence model: Reynolds Stress Turbulence (Linear Pressure Strain Two–Layer)
Advection scheme: 2nd order Upwind
Computational domain:

- Lateral direction: 4x4 rod bundle
- Axial direction: 2.65 m (Z/D = –58.5D, 45.8D)
- Heated rod: single rod (heated length = 400 mm)

Boundary conditions:

- Inlet: uniform velocity & temperature
- Outlet: uniform velocity
- Heated wall: constant heat flux

Meshing parameters:

Test	P/D	Mesh type	Number of cells	Number of prism layers	y^+_w @ z/D = 10
Isothermal test	1.35	Polyhedron	265M	8	0.1–1.0
	1.08	Polyhedron	182M	8	0.1–1.0
Heated–rod test	1.35	Polyhedron	280M	8	0.1–1.0
	1.08	Polyhedron	190M	8	0.1–1.0

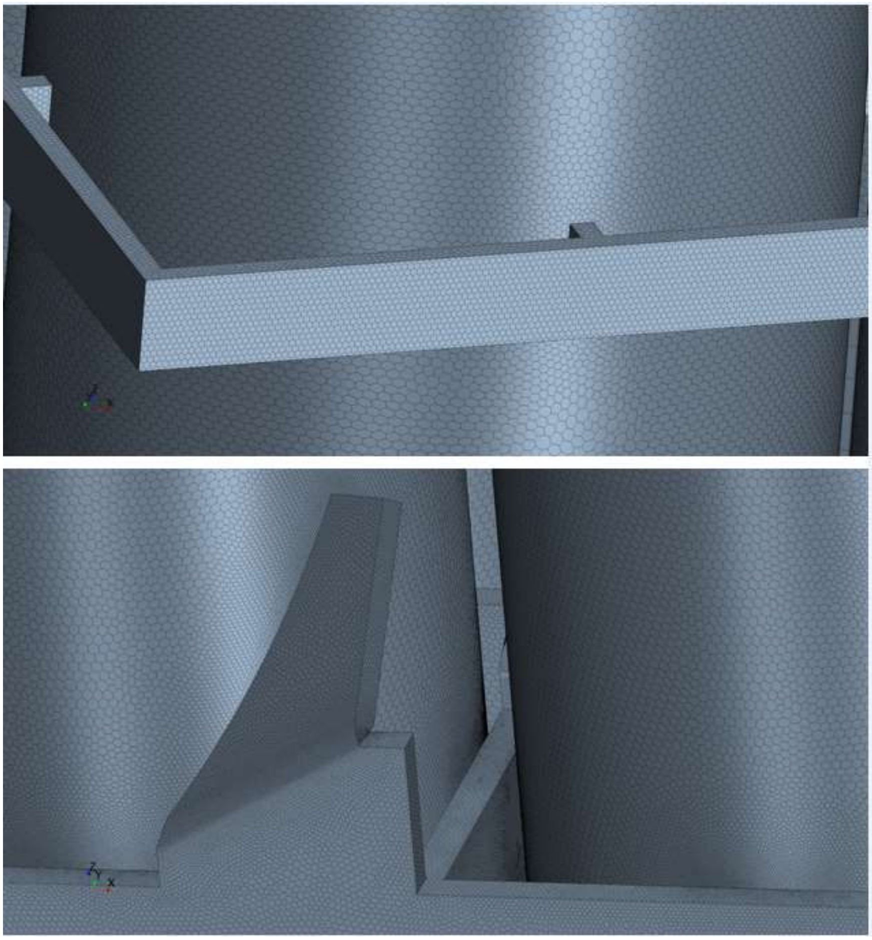

FIG. 41. Polyhedral mesh for STAR–CCM+ (182M, P/D = 1.08).

4.

5. SYNTHESIS OF THE BUNDLE BENCHMARKS

5.1. FLOW MIXING BENCHMARK

KAERI provided both the experimental conditions and results for flow mixing in rod bundle to the CRP participants. The CRP participants performed the CFD analysis using the KAERI data and submitted their CFD results. The data requested for this benchmark are the axial and lateral velocity profiles in the central subchannel of 4x4 rod bundle, which had to be provided following a template prepared by KAERI. The template allows to compare the CFD predictions for mean and RMS axial velocity with the experimental results, which report the axial variations at the subchannel center and gap, indicated below. Figure 42 shows a sample template for the mean and RMS axial velocity (W & Wrms) downstream of the twist–vane grid (z/D). The mean and RMS lateral velocities were requested along the horizontal centerline in the central subchannel at various axial locations downstream of the vane grid (z/D = 1.4, 3, 6, 10, 14, 20).

Figure 43 shows a sample template for the mean and RMS lateral velocity (V & Vrms) along the horizontal centerline (x) at a specified axial location. The coordinate x represents the horizontal axis and the position of x = 0 indicates the origin of central subchannel. The coordinate system is displayed in Fig. 8. It was also requested to provide the mean crossflow velocity (U) in the left gap of central subchannel at various axial locations downstream of the vane grid (z/D = 1.4, 3, 6, 10, 14, 20). The crossflow velocity was requested only for regular bundle. The template for the crossflow velocity is illustrated in Fig. 43. The coordinate y represents the lateral axis, which is vertical to horizontal axis(x), and the position of y = 0 indicates the center of left gap in vertical direction. The gap width is 8.9 mm for regular bundle.

z/D(CFD)	W(CFD)	Wrms(CFD)
1.00	1.16831	0.248556
1.25	1.15064	0.23692
1.50	1.24471	0.226035
1.75	1.25315	0.217861
2.00	1.29525	0.213615
2.25	1.34866	0.211142
2.50	1.38947	0.208775
2.75	1.43099	0.206359
3.00	1.4708	0.204405
3.25	1.51025	0.202373
3.50	1.5507	0.199284
3.75	1.58567	0.195611
4.00	1.61929	0.190498
4.25	1.64864	0.184328
4.50	1.6737	0.17741
4.75	1.69516	0.169987
5.00	1.71377	0.162523
5.50	1.74544	0.148318
6.00	1.76557	0.136731
6.50	1.78093	0.127117
7.00	1.79238	0.119389
7.50	1.80118	0.113145
8.00	1.80726	0.108049
8.50	1.8102	0.103905
9.00	1.8106	0.100533
9.50	1.80945	0.0977606
10.00	1.80779	0.0953863

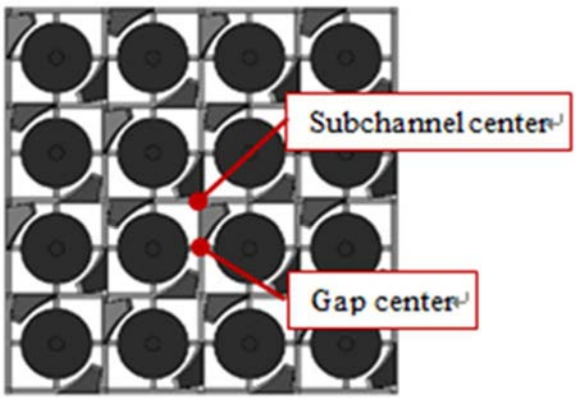

<Measuring position of axial velocity by LDV>

FIG. 42. Sample template for the mean and RMS axial velocity at the subchannel center and gap.

x(CFD)	V(CFD)	Vrms(CFD)
-17.0	0.06504	0.13436
-16.0	-0.0088	0.14189
-15.0	-0.0758	0.14695
-14.0	-0.1483	0.15242
-13.0	-0.226	0.15011
-12.0	-0.2916	0.14698
-11.0	-0.3023	0.14691
-10.0	-0.3102	0.14697
-9.0	-0.3281	0.15138
-8.0	-0.3526	0.15773
-7.0	-0.4577	0.15823
-6.0	-0.5421	0.16196
-5.0	-0.5928	0.17166
-4.0	-0.6042	0.18576
-3.0	-0.5246	0.2033
-2.0	-0.4191	0.21993
-1.0	-0.2054	0.23033
0.0	0.0216	0.22962
1.0	0.23838	0.22419
2.0	0.4242	0.21119
3.0	0.53293	0.19607
4.0	0.60125	0.18191
5.0	0.58318	0.17089
6.0	0.55509	0.1611
7.0	0.47556	0.15641
8.0	0.39239	0.15112
9.0	0.35174	0.14838
10.0	0.31635	0.14528
11.0	0.29713	0.14544
12.0	0.27548	0.14576
13.0	0.19717	0.15082
14.0	0.12706	0.15087
15.0	0.056	0.14545
16.0	-0.013	0.14115
17.0	-0.0795	0.13778

y(CFD)	U(CFD)
-4.0	-0.2232
-3.5	-0.1712
-3.0	-0.1738
-2.5	-0.1939
-2.0	-0.2546
-1.5	-0.3175
-1.0	-0.3721
-0.5	-0.4183
0.0	-0.4628
0.5	-0.5032
1.0	-0.5328
1.5	-0.5557
2.0	-0.5786
2.5	-0.5982
3.0	-0.6222
3.5	-0.6447
4.0	-0.6707

FIG. 43. Sample templates for the mean and RMS lateral velocity along the hrozontal centerline (V & Vrms), and the mean crossflow velocity in the left gap (U).

The mean axial velocity (Wm) predictions at the subchannel center are compared in Fig. 44 for the regular bundle (P/D = 1.35). The SJTU prediction appears to be in excellent agreement with the experimental results. While such close agreement could be attributed to the adoption of fine hexa–dominant mesh, which had evidenced optimal performance in conjunction with finite volume solvers at previous fuel benchmarks, the very close agreement opens some uncertainty and it was agreed in the 4th RCM (November 7–10, 2017) that the SJTU will conduct an independent CFD analysis to confirm the first calculation, hence the SJTU results will not be extensively discussed in this synthesis report. The BARC and KAERI calculations show the mean axial velocity profiles in reasonable agreement with the experimental data, where BARC adopted the SST k–w model and KAERI used Realizable k–ε model. The NPIC and VNIIAES calculations show a large under–prediction near downstream of the spacer grid (z/D < 3). Further downstream of the grid (z/D > 4), the CFD calculations for the axial velocity profiles agree well each other, showing very little influence of turbulence models and solution methods, and in reasonable agreement with the measured velocity profile.

Figure 45 shows the comparison of the mean axial velocity profiles in the gap for the regular bundle (P/D = 1.35). All the CFD calculations, with exception for the SJTU results, somewhat under–predict the velocity profiles, but produced mostly similar results with reasonable agreement with the measured data. The BARC and KAERI predictions show good agreement far downstream (z/D > 6). The SJTU result will be confirmed later based on independent simulations.

The axial RMS velocity (Wrms) profiles are compared in Fig. 46 for the regular bundle. In general, the CFD calculations predict lower RMS velocity than the measured one. The CFD predicts a faster turbulence decay in the first 4–5 z/Ds at the subchannel center, which leads to similarly low turbulence level predictions further downstream (z/D > 6) for all models. The predictions of the RMS levels at the gap center are somewhat different, the VNIIAES calculation shows a reasonable agreement with the experimental result. The VNIIAES used the 2nd–order turbulence model (Reynolds stress model) with the polyhedral cells of more than 200M. It is also noted that the CFD calculations show better agreement for the RMS axial velocity in the gap than the result in the subchannel center.

The mean axial velocity profiles for the tight lattice bundle (P/D = 1.08) are compared in the subchannel center and the gap as shown in Figs. 47 and 48. The CFD calculations of axial velocity in the subchannel center in Fig. 47 show that the computed profiles have similar trends for (z/D < 4), although with interestingly different absolute values, and which agrees with the measured result. Larger variations exist in the near spacer region, where the BARC calculation shows the better prediction of axial velocity in the subchannel center. The VNIIAES results show a rapid decrease of axial velocity in the subchannel center far downstream (z/D > 8). The mean axial velocity in the gap (Fig. 48) shows a larger discrepancy between the CFD calculations and the experimental result. The CFD calculations predicted a significantly larger variation (e.g., 1.0 – 2.0 m/sec) downstream of the vane grid than the measured one (e.g., 1.5 – 1.8 m/sec).

Figure 49 compares the RMS axial velocity profiles in the subchannel center and gap for the tight lattice bundle. The CFD calculations show turbulence levels that are significantly lower than the experimental results, especially immediately downstream the vane grid (z/D < 4). The BARC and NPIC calculations show better predictions in the subchannel center. The measured RMS velocity in the subchannel center changes from 0.4 m/sec at z/D = 2 to 0.15 m/sec at z/D = 10. The BARC prediction changes from 0.3 m/sec at z/D = 2 to 0.1 m/sec at z/D = 10. The measured RMS velocity in the gap is almost twice those produced by the CFD calculations, while there is no significant difference between the CFD calculations for the RMS velocity in the gap.

The mean lateral (vertical) velocity (Vm) profiles along the horizontal centerline in the central subchannel are compared in Fig. 50 for the regular bundle (P/D = 1.35). The mean vertical velocity (Vm) shows a symmetric profile from the subchannel center (x = 0) due to a swirl caused by the twist–vane. The CEA, KAERI and NPIC calculations show double peaks of velocity profile near downstream (z/D = 1.4) which agrees well with the measured profile. The CFD calculations except for the VNIIAES one predicts the velocity profile which reasonably agrees with the measured one. The VNIIAES calculation predicts somewhat higher vertical velocity. The KAERI predictions show excellent agreement with the experimental result. The BARC and NPIC calculations also show a good agreement for the vertical velocity far downstream, e.g., z/D = 10 and 20.

The RMS lateral (vertical) velocity (Vrms) profiles along the horizontal centerline in the central subchannel are compared in Fig. 51 for the regular bundle (P/D = 1.35). The experimental and CFD results show a symmetric profile along the subchannel center (x = 0). The CFD calculations show RMS velocities significantly lower than the measured one. The VNIIAES calculation correctly predict the RMS peak just downstream of the spacer (z/D = 1.4) at the subchannel center. Further downstream (z/D = 10) none of the simulations seem to predict the central peak, while showing small differences between the various solutions, with the NPIC profile being somewhat closer to the experiments. In general, the difference between the CFD calculations and measurements for the RMS velocity is quite large far downstream of the spacer.

The mean crossflow velocities (Um) in the left gap of the central subchannel are compared in Fig. 52 for the regular bundle. The CFD calculations show asymmetric crossflow profiles which agrees well with the experimental results. The difference between the CFD calculations appears to be larger further downstream (z/D = 6). There is no significant difference between the CFD calculations (except for the VNIIAES one) and the measured data for the crossflow near downstream (z/D = 1.4), which is introduced by the twist–vanes, with a small exception for the VNIIAES calculation where the second order turbulence model adds turbulence driven secondary flows to the crossflows deriving from the twist vanes. Figure 53 shows the comparison of mean lateral (vertical) velocities (Vm) in the central subchannel for the tight lattice bundle (P/D = 1.08). The CFD predictions show vertical velocities higher than the experimental result. The maximum vertical velocities just downstream of the spacer (z/D = 1.4) are 0.4 m/sec and 0.7 m/sec for the experiment and the CFD calculations, respectively. The peak velocity occurs closer to the center (x = 0) in the CFD calculations (x = –3 & 3), in contrast to the experimental case (x = –6 & 6). The KAERI and NPIC cases show almost the same predictions. The BARC calculation shows the highest peak velocity at the z/D = 1.4 location, while the VNIIAES results predict the highest peak velocity further downstream (z/D = 6). It is noted that the CFD calculations for tight lattice bundle show mean vertical velocities that are significantly higher than the CFD cases for regular bundle.

Figure 54 compares the RMS lateral velocities (Vrms) in the central subchannel for the tight lattice bundle (P/D = 1.08). The experimental result shows a parabolic profile with the peak value at the center (x = 0). Immediately downstream of the vane grid (z/D = 1.4), the measured values of Vrms are 0.5 m/sec in the center and 0.3 m/sec in the gap region (x < –10 & x > 10). The CFD calculations produce RMS velocities that are significantly lower than the experimental result particularly in central region of the subchannel, i.e., –5 < x < 5. The CFD predictions show a large difference at the near location (z/D = 1.4), which is reduced further downstream but still inconsistent with the measurements (z/D = 6).

Summary of the flow–mixing benchmark

1. The mean axial velocities (Wm) were compared in Fig. 44 – Fig. 45 and Fig. 47 – Fig. 48 for regular and tight lattice bundles, respectively. The CFD calculations showed profiles of Wm which reasonably agreed with the experimental results in the subchannel center and gap for regular bundle. For tight lattice bundle, while the CFD calculations showed acceptable agreement with the measured one in the subchannel center, a somewhat larger discrepancy (under–prediction) was observed in the gap region.

2. The RMS axial velocities (Wrms) were compared in Figs. 46 and 49 for regular and tight lattice bundle, respectively. For the regular bundle, the CFD calculations showed generally lower values of Wrms in comparison to the measured data, and better

agreement for the Wrms in the gap region than in the subchannel center. The CFD calculations produced significantly lower RMS velocities in comparison to the experimental results for the tight lattice bundle.

3. The mean lateral velocities (Vm) in the central subchannel were compared in Fig. 50 (regular bundle) and Fig. 53 (tight lattice bundle). For regular bundle geometry the CFD calculations predict the lateral velocities in close agreement with the experimental data, with exception of the Reynolds stress model results from VNIIAES. The CEA, KAERI and NPIC calculations all reproduced correctly the double peaked velocity profile for both grid spacer location (z/D = 1.4 and z/D = 20). In contrast, for the case of the tight lattice bundle, the CFD predictions show significantly higher velocity predictions in comparison to the experimental result.

4. The RMS lateral velocity predictions (Vrms) are compared in Fig. 51 (regular bundle) and Fig. 54 (tight lattice bundle). The CFD predictions of the RMS velocities are significantly lower than the experimental result, particularly in the central region of the subchannel. The difference between the CFD predictions and the measured RMS velocity is particularly evident at the first measurement location downstream the spacer, with a partial recovery further downstream.

   It is noted that the design of the spacers included small cylindrical support structures in place of common spring and dimple designs adopted in commercial fuel spacers. Such supports are expected to produce a considerable amount of flow shedding and contribute to increased values for the RMS of velocity just downstream of the spacer. As all the simulations compared did not resolve the local shedding, could partly explain the large differences encountered.

5. The mean crossflow velocities (Um) in the left gap of the central subchannel are compared in Fig. 52 for the regular bundle. The CFD calculations show asymmetric crossflow profiles which agree well with the experimental results. The difference between the CFD calculations appears to somewhat increase further downstream (z/D = 6).

6. It is somewhat surprising that some participants still adopt hybrid tetra meshes in combination with finite volume solvers, while at least trying to limit the tetra meshes to the spacer region. Such combination has been proven to be not ideal, and to introduce excessive numerical dissipation and is strongly discouraged. Further, the flow in a fuel assembly is mostly aligned along the axial coordinate, which gives strong advantage to computational cells that are aligned with the flow in reducing numerical error. Past fuel benchmarks, including the recent EPRI industrial benchmark [9], [10] have further demonstrated the advantage of hexa–dominant meshes in simulation single phase fuel applications.

7. Some of the participants have tried to leverage the ‘hybrid’, ‘all yplus’ or ‘scalable’ character of recent commercial implementation of turbulence models for the near wall treatment. Such approaches however should be assessed carefully before being leveraged, as most implementations in fact introduce largest errors for $5 < y^+_w < 20$.

8. While it was decided that the SJTU calculations will be reassessed independently, the shown accuracy would support the importance of hexa or hexa–dominant meshes, as their submission was the only one adopting such approach.

9. The comparison of the results evidences that the mesh quality appears to dominate over the specific selection of the Eddy Viscosity model. In the future, assessment of the influence of turbulence models on consistently assessed computational meshes would allow a more valuable evaluation of the models Based on the current results and assuming the validity of the SJTU results, combination of fine Hexa–dominant meshes with the Realizable k–ε model produces best results for the isothermal bundle benchmark. The SJTU calculation will be evaluated later based on the follow–up simulation in SJTU.

10. While anisotropy of the flow is expected to play a role in the simulations, application of a standard RSM model (details to be better clarified) by the VNIIAES leads to large error in the predictions. This is again consistent with previous experiences, where non–linear eddy viscosity models showed to provide more robust predictions in fuel related simulations [9] ,[10], [11], [12].

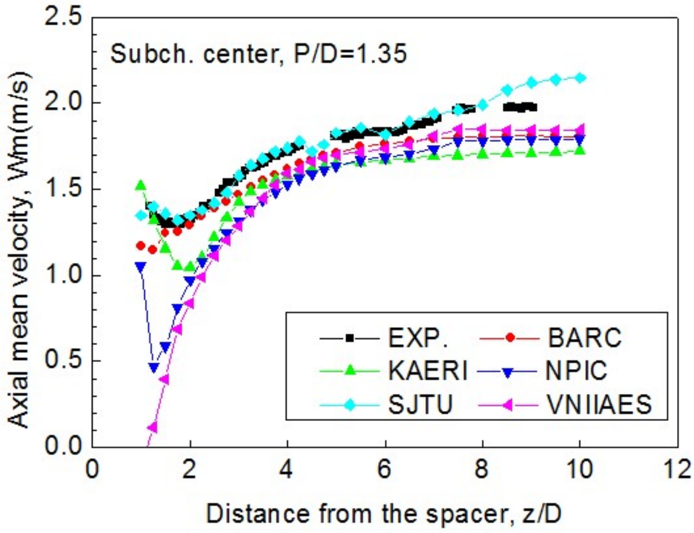

FIG. 44. Comparison of mean axial velocity at the subchannel centre for regular bundle.

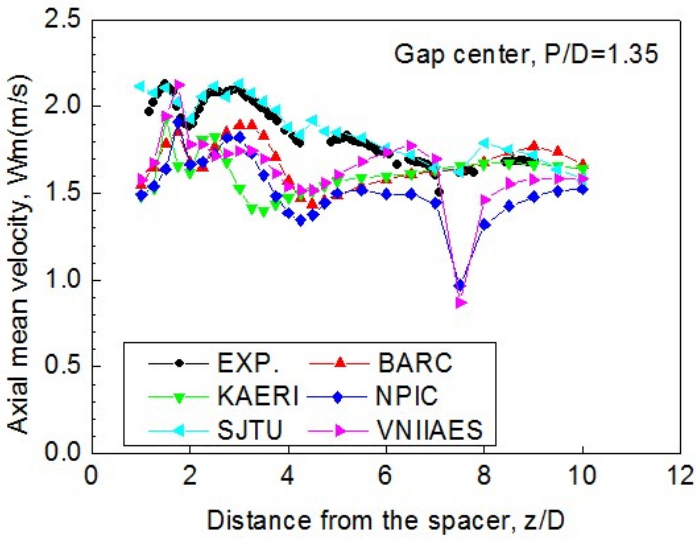

FIG. 45. Comparison of mean axial velocity in the gap for regular bundle.

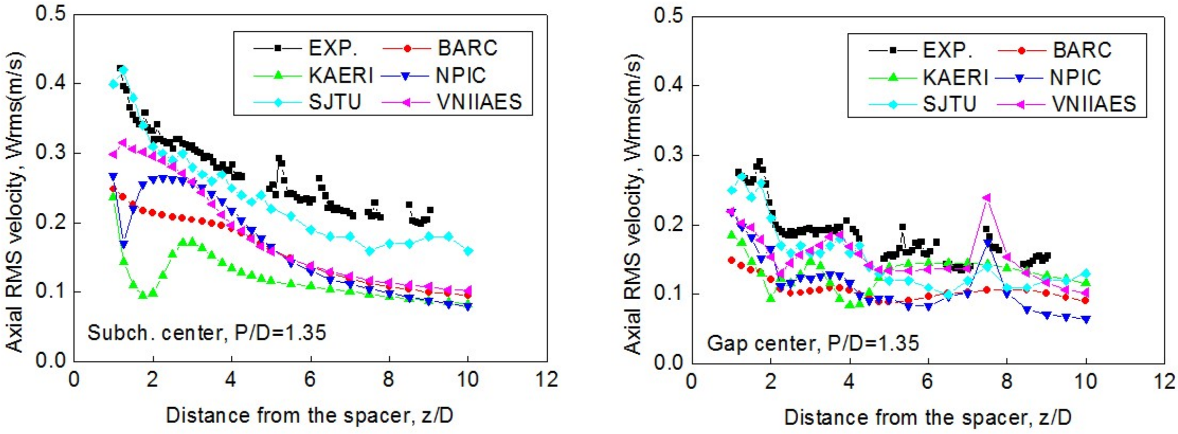

FIG. 46. Comparisons of RMS axial velocity in the subchannel centre and gap for regular bundle.

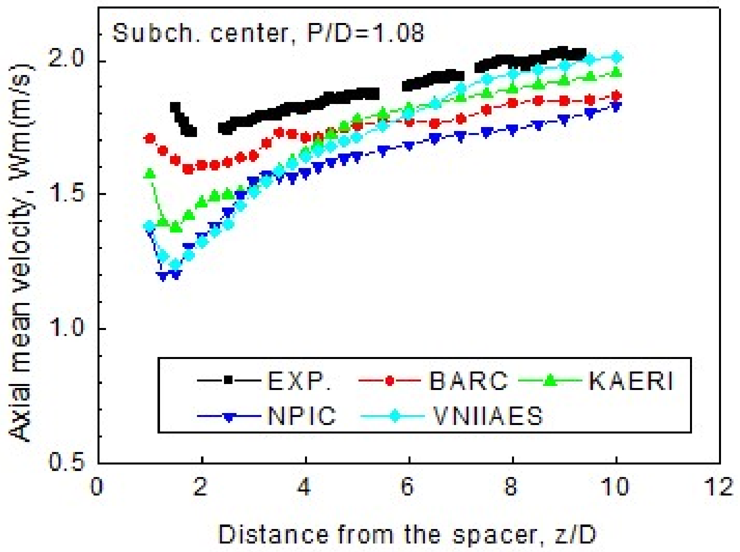

FIG. 47. Comparison of mean axial velocity at the subchannel centre for tight lattice bundle.

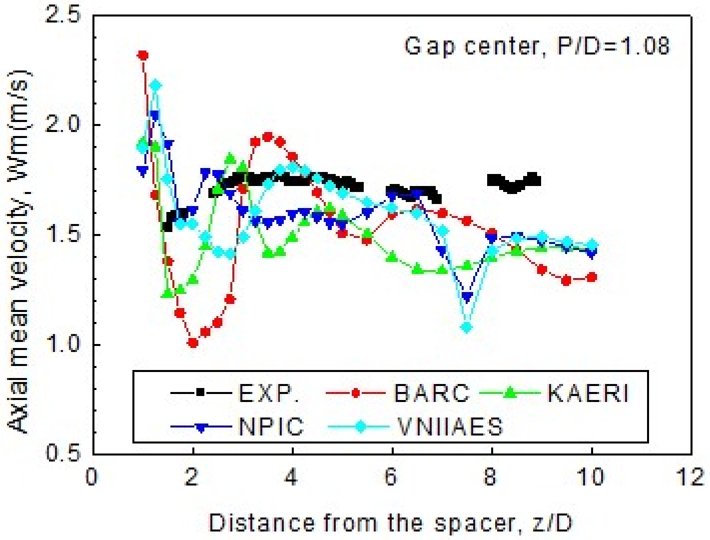

FIG. 48. Comparison of mean axial velocity in the gap for tight lattice bundle.

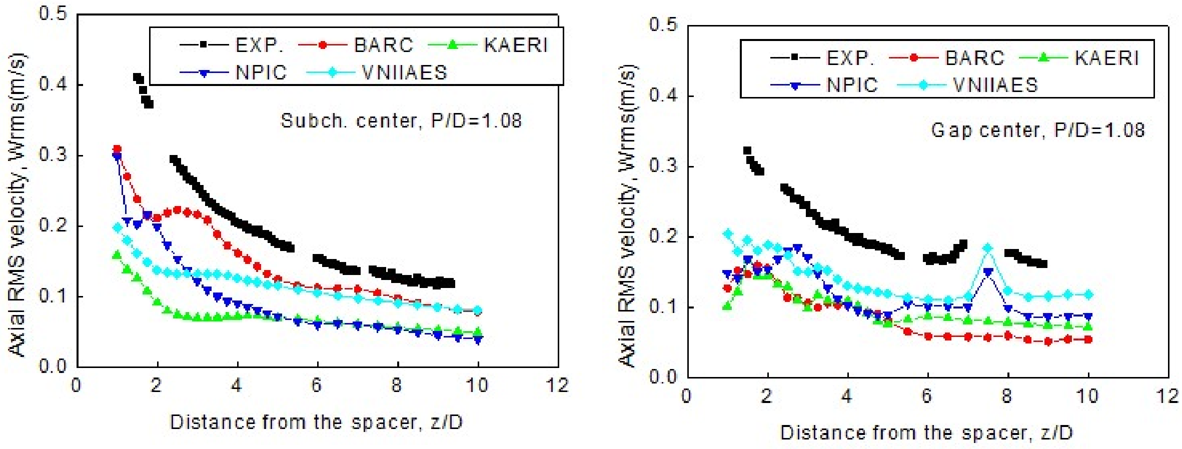

FIG. 49. Comparisons of RMS axial velocity in the subchannel centre and gap for tight lattice bundle.

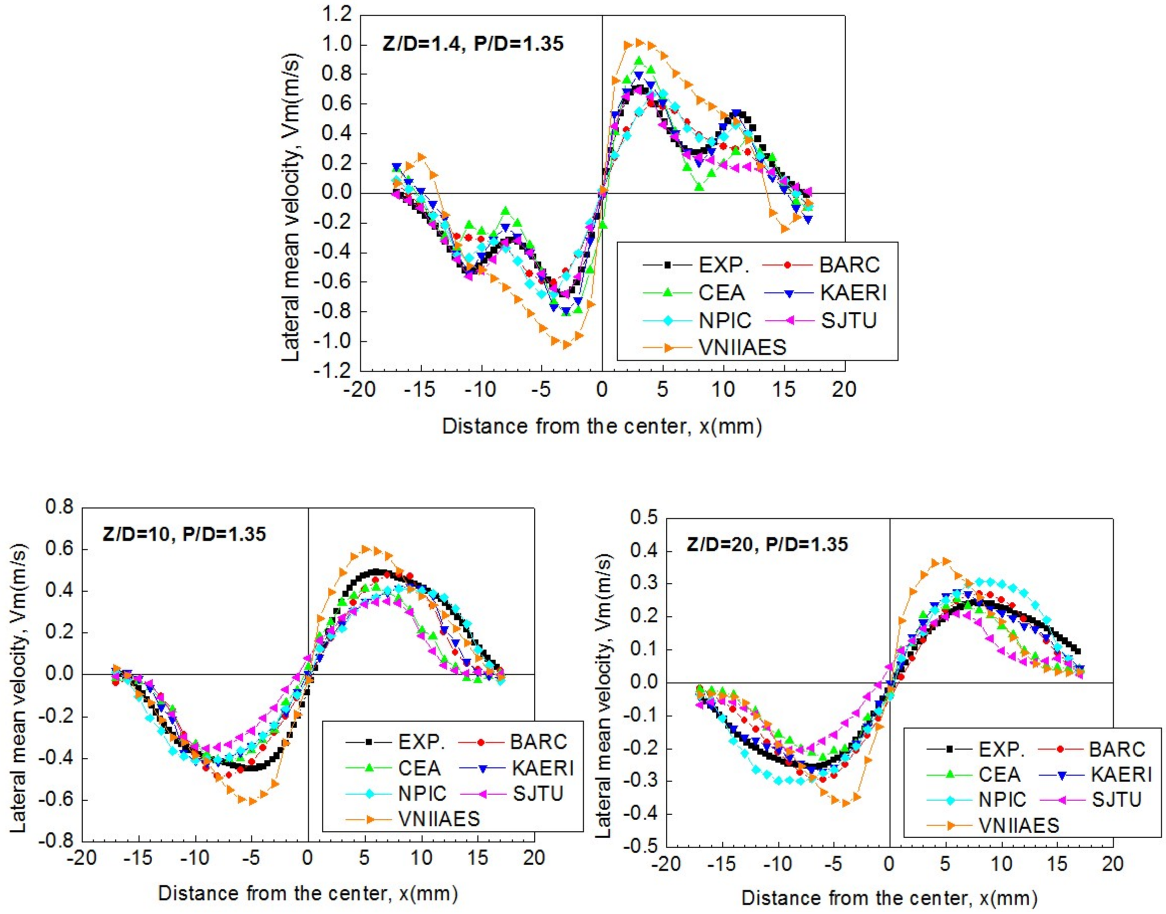

FIG. 50. Comparisons of mean lateral velocity in the central subchannel for regular bundle.

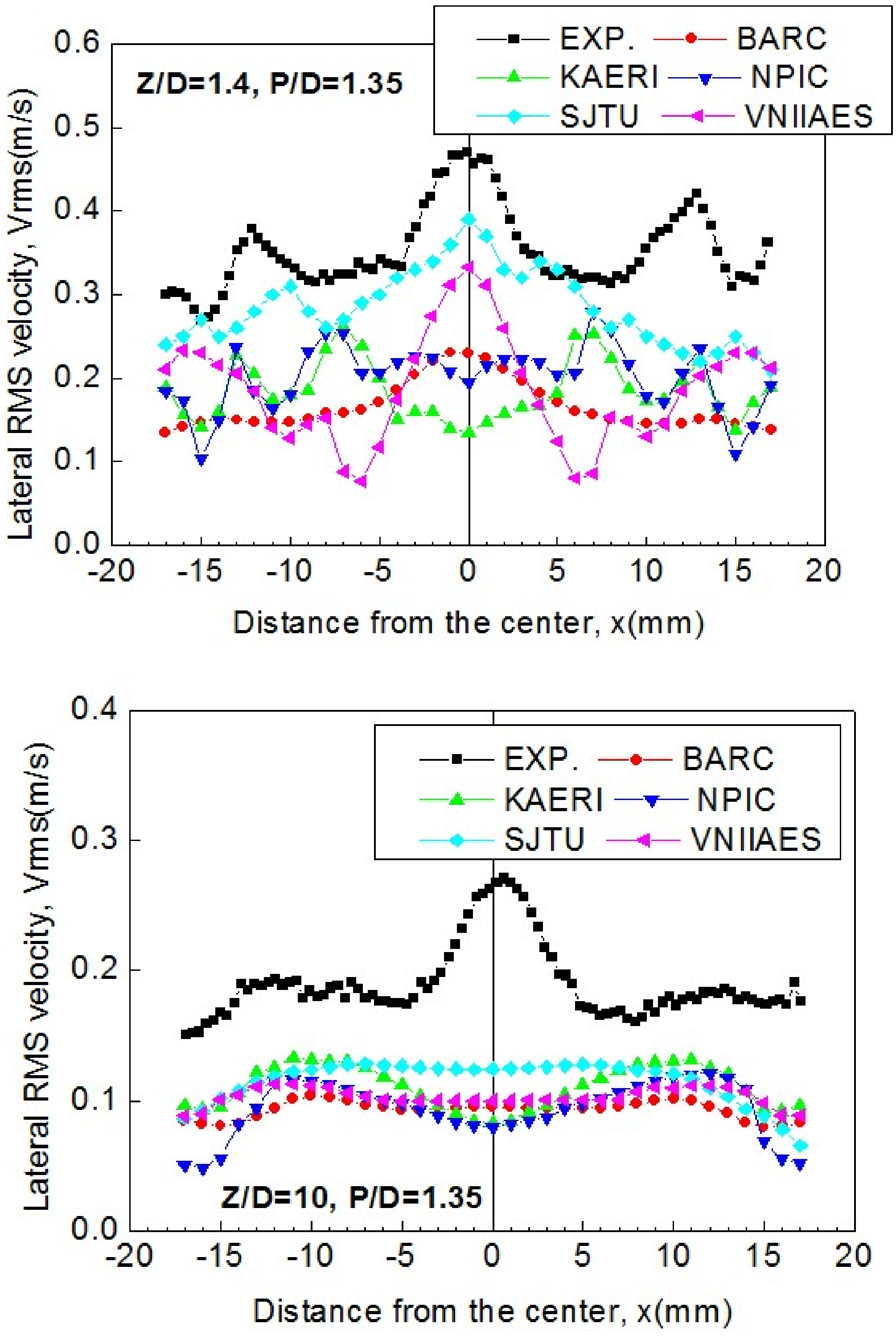

FIG. 51. Comparisons of RMS lateral velocity in the central subchannel for regular bundle.

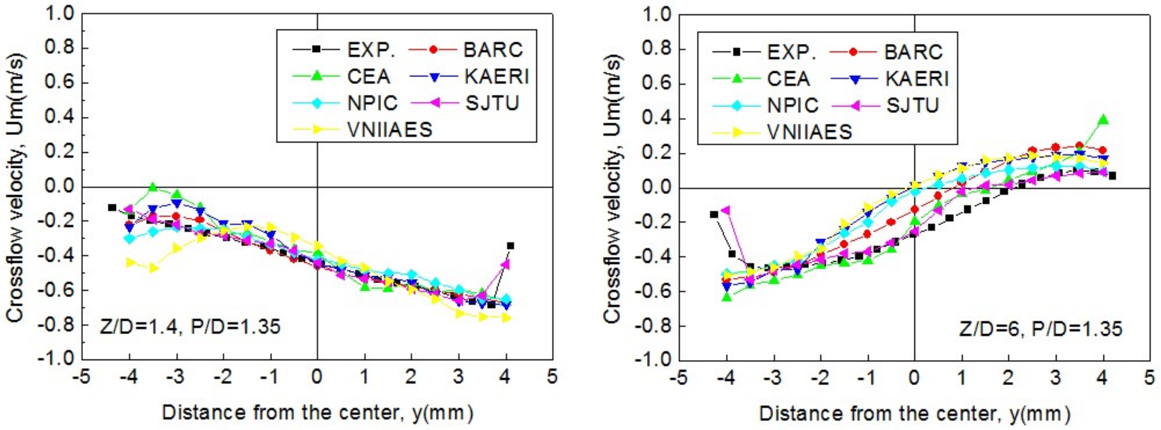

FIG. 52. Comparisons of crossflow velocity in the central subchannel for regular bundle

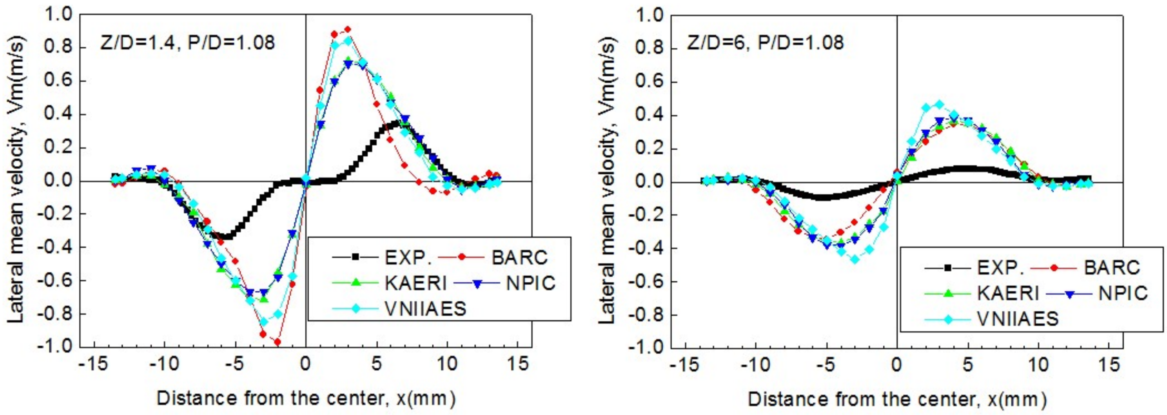

FIG. 53. Comparisons of mean lateral velocity in the central subchannel for tight lattice bundle

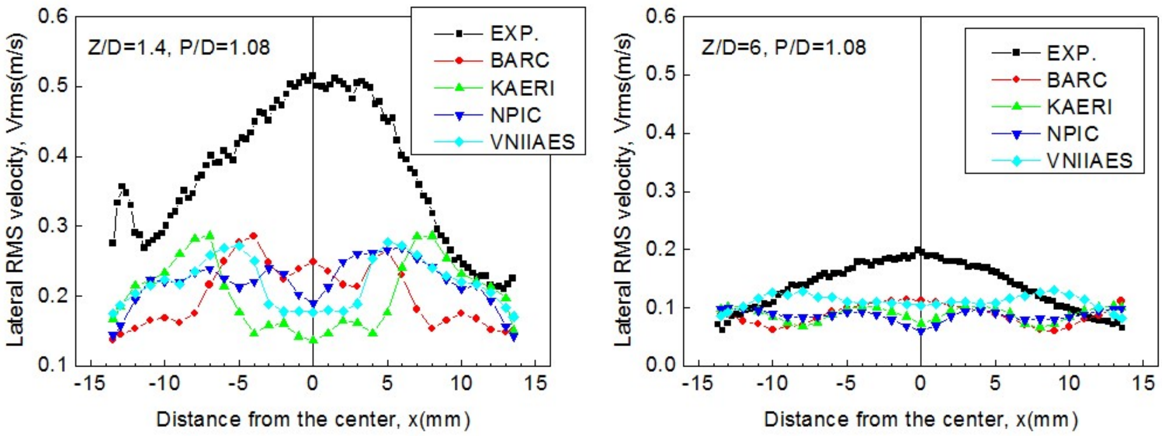

FIG. 54. Comparisons of RMS lateral velocity in the central subchannel for tight lattice bundle.

5.2.HEAT TRANSFER BENCHMARK

In the benchmark, KAERI also provided to the CRP participants detailed experimental conditions and results for heat transfer in a 4x4 rod bundle. The requested data were the circumferential variation of wall temperature for a heated rod, for both a regular and a tight lattice 4x4 rod bundle configurations. Again, KAERI prepared a template to request the CFD results. The template for this benchmark allowed comparing the CFD predictions with the experimental results for the rod wall temperatures. Figure 55 shows a sample template for both regular and tight lattice bundles, downstream of the twist–vane grid (z/D) and for varying azimuthal angles. The difference between wall temperature and fluid temperature (DTw) is requested for heated rod at various azimuthal and axial locations downstream of the vane grid. The azimuthal angle (θ) is 0, 22.5, 45, 67.5 and 90 for DTw1, DTw2, DTw3, DTw4 and DTw5, respectively.

Figure 56 shows the comparison of wall temperatures in the azimuthal direction at various downstream locations (z/D = 1.5, 3, 10) for the regular bundle. The SJTU result will not be discussed in this benchmark until an independent calculation is completed. The CFD calculations by BARC, CEA, KAERI and VNIIAES show reasonable agreement with the measured wall temperature immediately downstream (z/D = 1.5) of the spacer. The difference between the CFD prediction and the experimental result is less than 2 ^{O}C in the central region ($20 < \theta < 70$) and increases up to 4 ºC in the gap region. The comparisons at z/D = 3 and 10 show a larger disagreement between the various CFD calculations, and for some of them also a larger disagreement with the measured temperatures. The trend is even more evident far downstream of the spacer (z/D = 10). The BARC and CEA calculations produce a somewhat closer agreement with the measured temperature for the regular bundle. The combined effects of mesh and numerical methods, turbulence models and near wall treatment all play an important role in the heat transfer predictions. From the present results it is not possible to derive a straightforward understanding of the influence of the models, which might be overwhelmed by the numerical effects and possibly by interaction of the near wall treatment with the near wall mesh sizes. The twist–vane is expected to have an important effect in enhancing the heat transfer, generating strong swirl and crossflow immediately downstream of the spacer, which diminishes further downstream of the vane grid. It is expected that the influence of swirling is best represented by anisotropic turbulence models far downstream of the vane grid in rod bundle [13], [14], [15]. Hence, the effect of turbulence model increases far downstream. In the simulation BARC and KAERI used isotropic turbulence models (SST and Realizable k–ε), while CEA and VNIIAES used LES and RSM (which is expected to better account for the effects of anisotropy and swirling), respectively. However, the CEA and VNIIAES calculations did not show noticeably agreement with the experimental result in the far downstream region. It is therefore necessary to further investigate the details of the numerical methods and mesh convergence, and non–dimensional distance to the first cell from heated wall (y+w) in the future.

Figure 57 compares the axial variation of wall temperature (DTw2) downstream of the vane grid for the regular bundle. The BARC and CEA results again show somewhat closer agreement with the measured data, while the KAERI and VNIIAES calculations show large under–prediction. All the CFD calculations however predict the heat transfer enhancement well downstream of the twist–vane grid, in particular predicting incorrect trends in the region $2 < z/D < 5$. The decrease in wall temperature is 5 ºC and 2–4 ºC in the experiment and the CFD calculations, respectively. This corresponds to the heat transfer enhancement by 33 % and 17 %–40 %. The BARC predicts the 17 % and the KAERI predicts the 40 %.

The circumferential variations of wall temperature are compared in Fig. 58 for the tight lattice bundle. The measured temperature shows a circumferential variation immediately downstream of the spacer (z/D = 1.5) and 2 ºC further downstream (z/D = 3 & 10). The CFD calculations show considerably different predictions among the different participants, where the temperature variations range between 3 and10 ºC. The BARC and KAERI predictions agree well with the measured data for z/D = 1.5, but while the KAERI predictions continue to produce close agreement further downstream of the spacer, the BARC calculations shows a larger variation of wall temperature in downstream regions, i.e., z/D = 3 & 10. The CNL results predict wall temperatures that are much higher than the measured one. On the contrary, the VNIIAES results are significantly lower than the measured data. It is noted that the discrepancy between the CFD calculations and the experiment is larger for the tight lattice bundle than for the case of regular bundle.

Figure 59 compares the axial variation of wall temperature (DTw2) downstream of the vane grid for the tight lattice bundle. The KAERI calculations show good agreement with the experimental result while the BARC and VNIIAES calculations show large under–predictions. The CNL calculations show considerable over–prediction.

The KAERI participants further examined the effects of turbulence model employed, mesh type used (tetrahedral or polyhedral) and normal distance to the first cell from the heated wall (y+w). Figure 60 shows the effect of turbulence model for the circumferential variation of wall temperature in regular and tight lattice bundles. The KAERI calculations show a slight under–prediction in regular bundle but over–prediction in tight lattice bundle. The KAERI predictions using Realizable k–ε and SST k–w models agree reasonably with the experimental results. Figure 61 shows the effect of turbulence model on the axial variation of wall temperature. The difference between turbulence models appears to be insignificant in regular bundle. In the case of tight lattice bundle, the difference between turbulence models is larger and the SST k–w appears to better predict the measured data, but the results are strongly influenced by the finer resolution of the near wall mesh used with the SST model and a direct comparison cannot be made.

The effect of mesh type in Figs. 62 and 63 is apparent, and shows clearly improved prediction with the polyhedral cells in STAR–CCM+. The difference between polyhedral and tetrahedral cells is more significant in tight lattice bundle. Figure 64 shows the effect of dimensionless first–cell distance (y+w) from rod surface with SST k–w model for tight lattice bundle. The CFD calculation with a smaller value (1.5) of y+w tends to predict higher wall temperature and the difference becomes large far downstream (z/D = 10). The CFD prediction with y+w = 1.5 agrees well with the circumferential variation of wall temperature.

Summary of the heat–transfer benchmark

1. Circumferential variations of wall temperature were compared in Figs. 56 and 58 for regular and tight lattice bundle, respectively. The CFD calculations show reasonable agreement with the measured wall temperature immediately downstream the spacer but produce a larger disagreement further downstream (z/D > 1.5). The discrepancy between the CFD calculations and the experiment is larger for the tight lattice bundle than for the case of regular bundle.

2. The stream wise variations of wall temperature downstream of the twist–vane grid are compared in Figs. 57 and 59 for regular bundle and tight lattice bundle, respectively. All the CFD calculations predict the heat transfer relatively well. For the regular bundle, the BARC and CEA results show good agreement with the measured data, while the KAERI and VNIIAES calculations show large under–prediction. In the case of tight lattice bundle, the KAERI prediction agrees reasonably well with the experimental result while the other CFD calculations show larger under–predictions (BARC and VNIIAES) and over–prediction (CNL).

KAERI performed additional CFD analysis to examine the effects of turbulence model, mesh type and dimensionless wall distance (y^+_w). The difference between turbulence models is not clearly evident, while the effect of the near wall resolution is well evidenced. Adoption of y^+_w values of 10 is always discouraged and shows indeed negative effects on the predictions. The Realizable k–ε and SST k–w models overall agree reasonably well with the experimental results as shown in Figs. 60 and 61. On the other hand, the influence of the computational mesh is clearly evident, the CFD calculation with polyhedral cells provides clearly improved predictions in comparison to the case with tetrahedral cells (Figs. 62 and 63). The combination of SST k–w model and polyhedral cells with $y^+_w = 1.5$ in prism layers near the wall boundary gives best temperature predictions as shown in Figs. 61 and 64 (other combinations were not presented).

3. The results seem to underline that flow predictions have large effect on the temperature predictions. However, the calculation presented show an inconsistent combination of near wall models and meshing, which might be dominating the presented temperature predictions. While hybrid models (all–yplus, scalable wall functions etc.) are designed to reduce the inaccuracies across a range of non–dimensional wall distances, they still introduce large errors in the range $2 < y^+_w < 20$. The KAERI results in Fig. 64 further demonstrate this effect.

z/D	z(mm)	DTw1	DTw2	DTw3	DTw4	DTw5
1.5	38.1	12.4	11.5	12.9	14.3	14.7
2	50.8	11.7	10.2	12.8	14.6	14.7
2.5	63.5	11.5	10.3	12.6	14.2	14
3	76.2	12.1	10.8	12.7	14	14.1
5	127	13.8	12.3	13.6	15.1	15.5
10	254	16.3	13.6	15.7	17.8	16.1
12	304.8	16.7	14.6	16.5	17.1	16.4

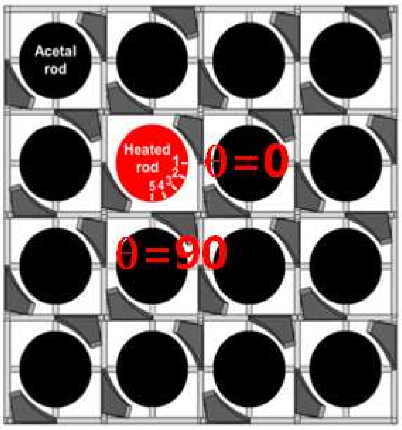

FIG. 55. Template for rod wall temperature and azimuthal coordinate.

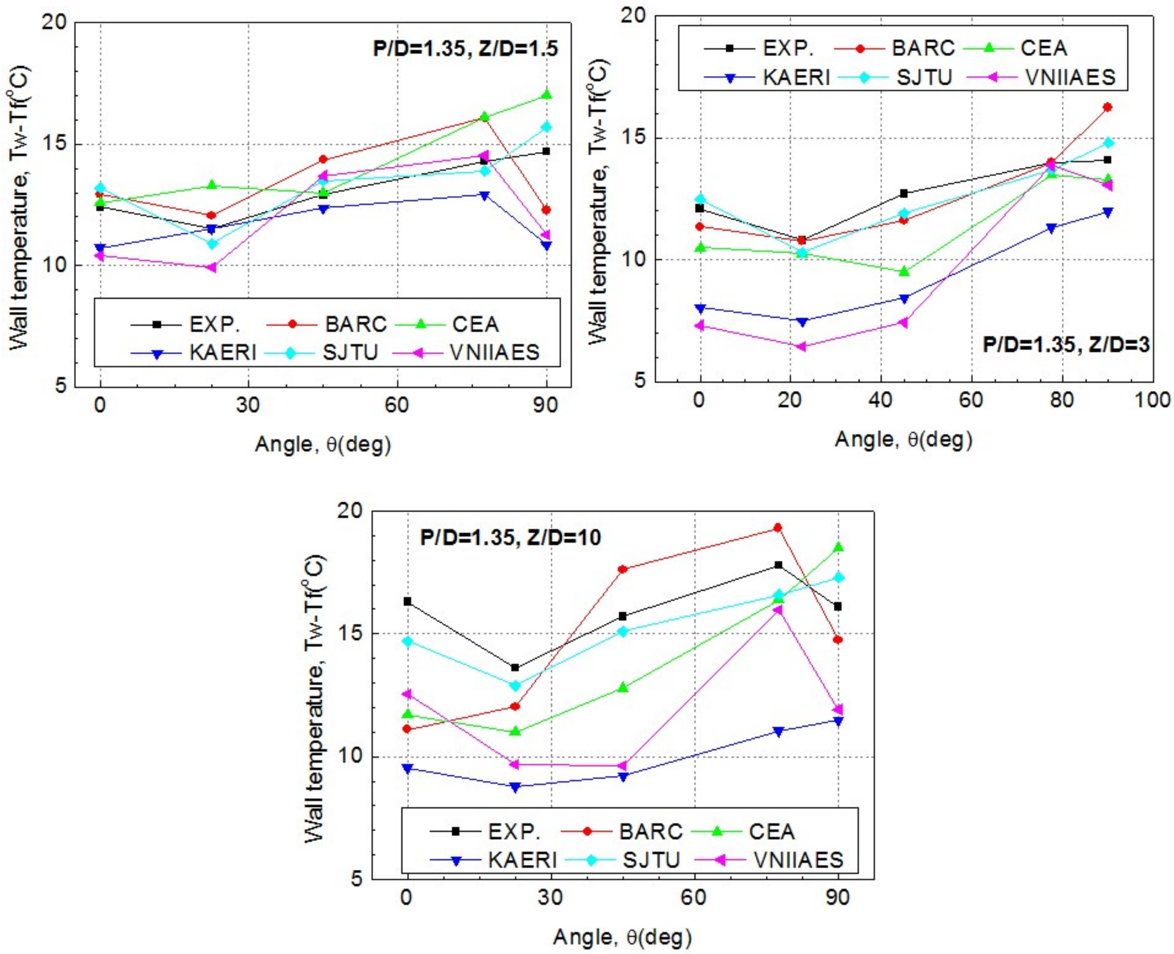

FIG. 56. Comparisons of wall temperature in azimuthal direction for regular bundle.

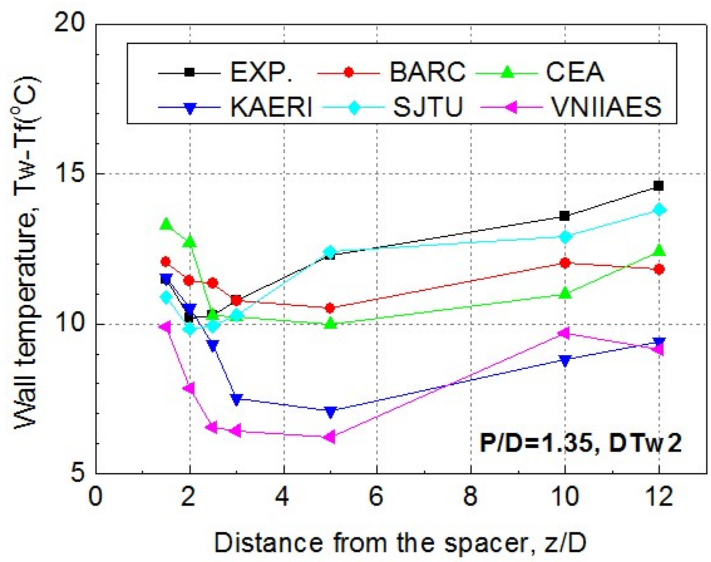

FIG. 57. Comparison of wall temperature in stream wise direction for regular bundle.

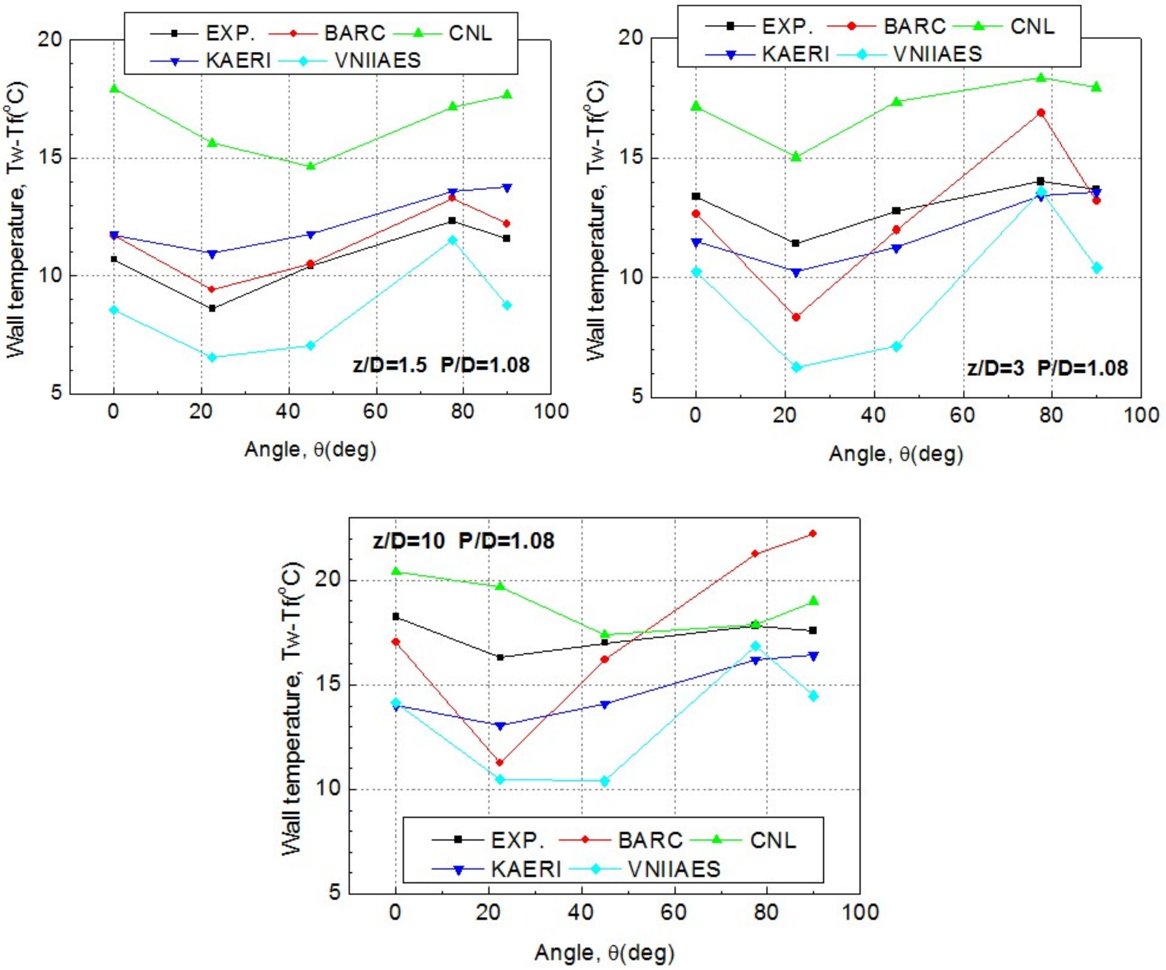

FIG. 58. Comparisons of wall temperature in azimuthal direction for tight lattice bundle.

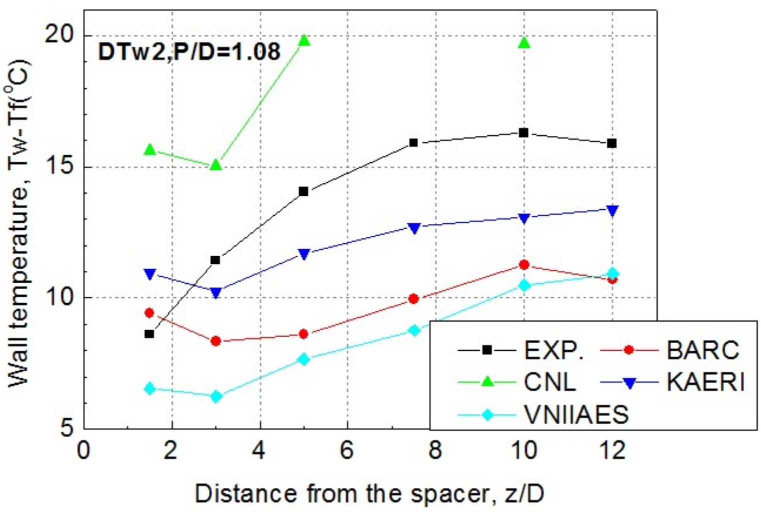

FIG. 59. Comparison of wall temperature in stream wise direction for tight lattice bundle.

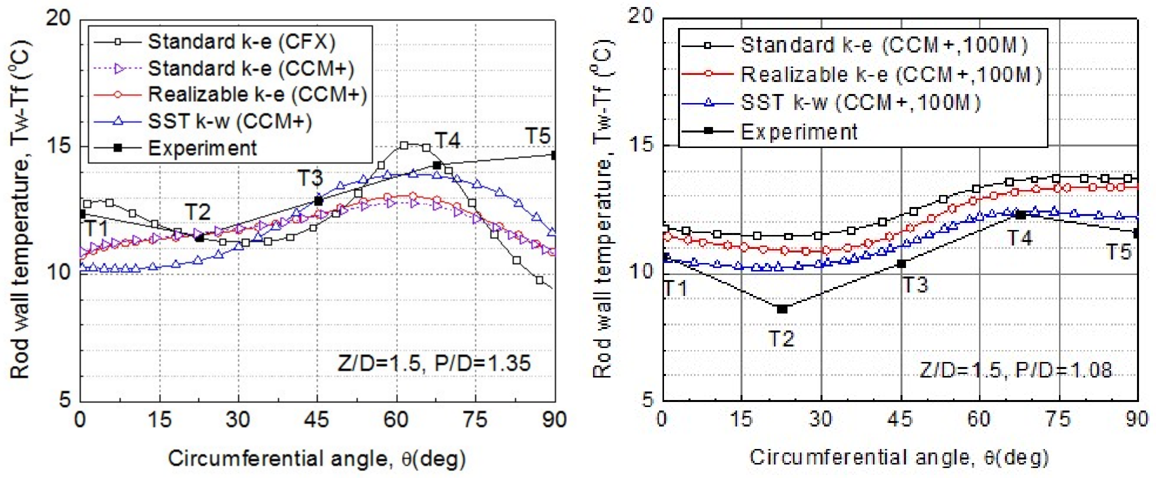

FIG. 60. Effect of turbulence model on circumferential wall temperature in regular and tight lattice bundles.

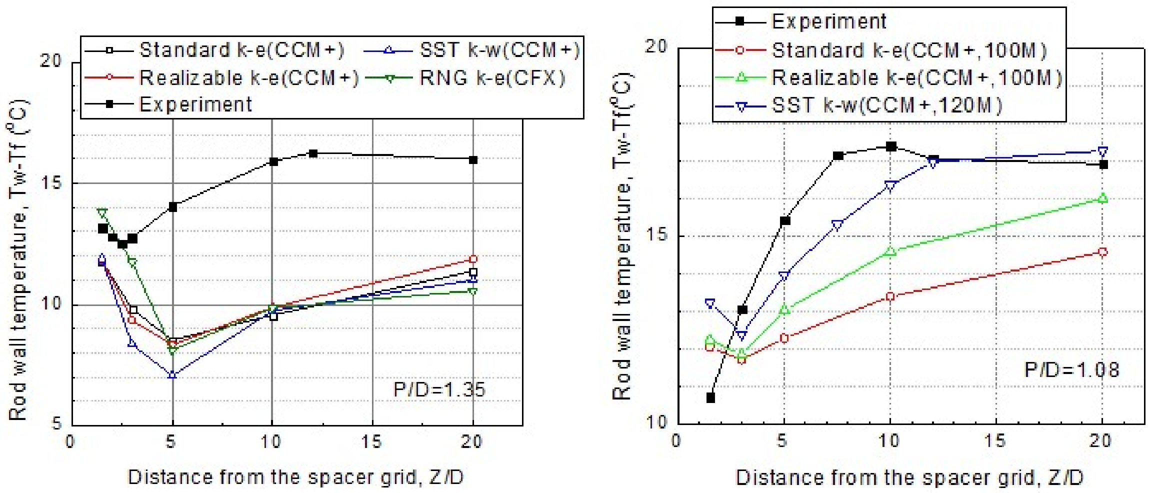

FIG. 61. Effect of turbulence model on axial wall temperature in regular and tight lattice bundles.

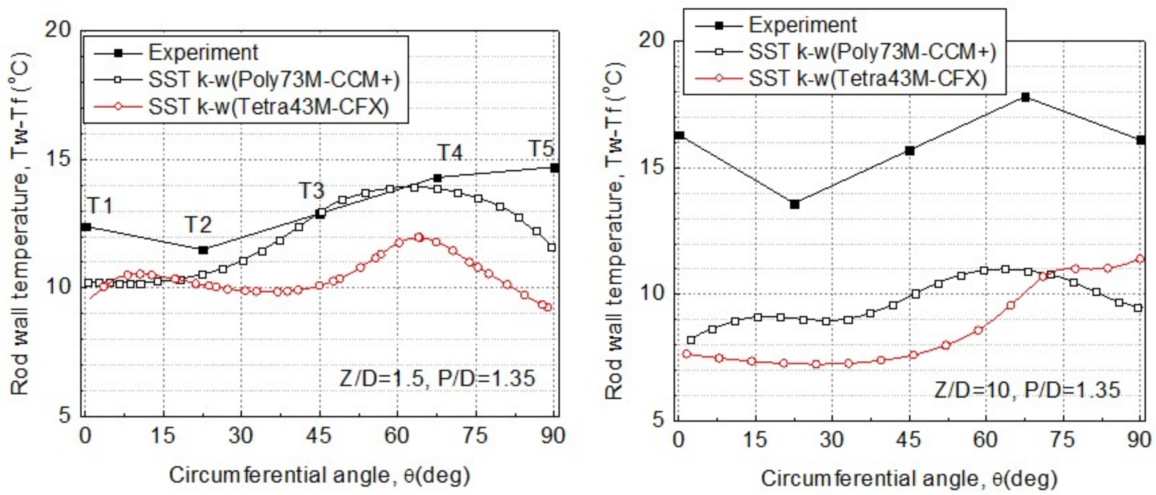

FIG. 62. Effect of mesh type on wall temperature in regular bundle.

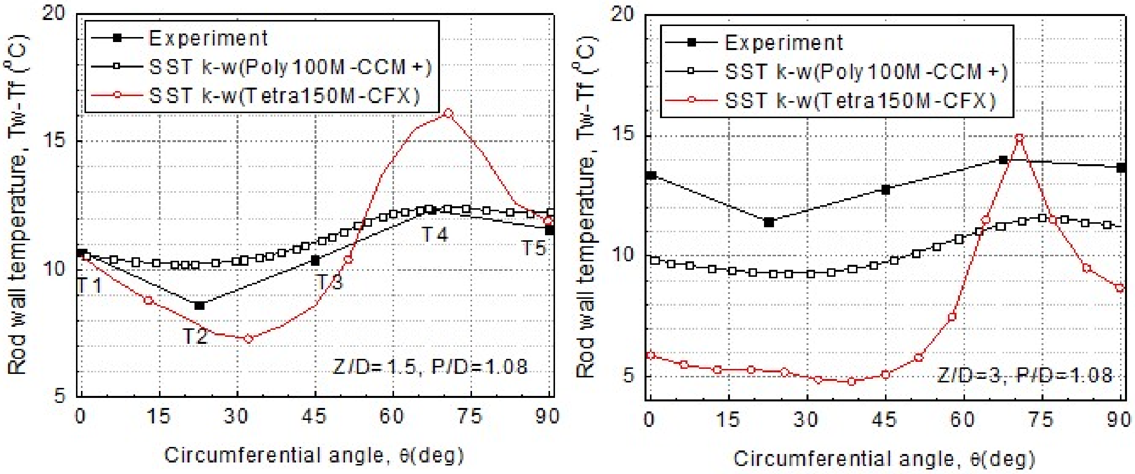

FIG. 63. Effect of mesh type on wall temperature in tight lattice bundle.

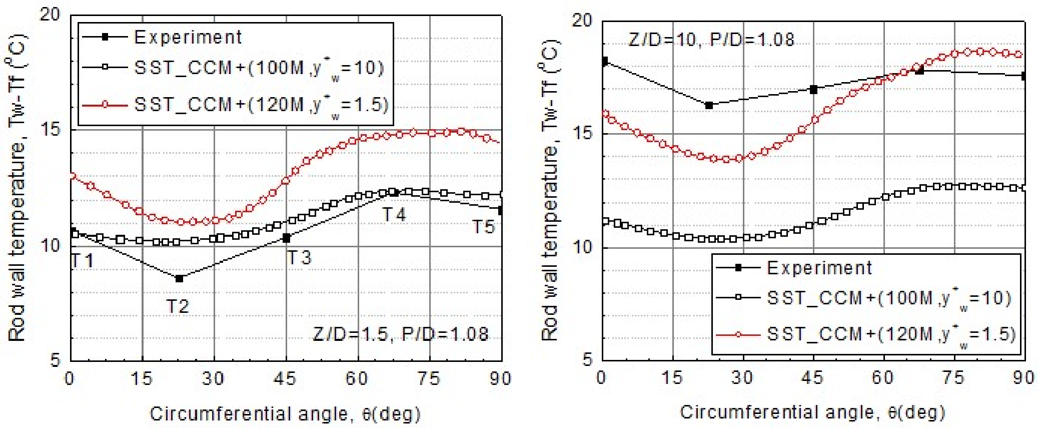

FIG. 64. Effect of dimensionless wall distance (y^+_w) on wall temperature in tight lattice bundle.

6. CONCLUSIONS

The IAEA has organized a Coordinated Research Project (CRP) on the application of Computational Fluid Dynamics (CFD) codes to Nuclear Power Plants (NPP) design. The rod–bundle tests carried out by the Korea Atomic Energy Research Institute (KAERI) were chosen as one of the benchmark tests for the verification and validation of CFD method in this IAEA CRP. The KAERI provided the CFD–grade experimental data on the velocity field from the PIV and LDV measurements of flow mixing and on the rod temperature from heat transfer test in rod bundle with the twist–vane grid. The test bundle is a 4x4 rod bundle with the pitch–to–diameter (P/D) ratios of 1.35 and 1.08. The bundle–flow velocity is 1.5 m/s and the surface heat flux in the heated rod is 104 kW/m2.

Seven organizations from six countries participated in the CFD benchmarks for isothermal and thermal KAERI bundle tests. BARC, CEA, KAERI, SJTU and VNIIAES submitted CFD results for both the isothermal and thermal bundle benchmarks. CNL submitted CFD result for the thermal bundle benchmark only and the NPIC submitted CFD result for the isothermal bundle benchmark only. The CFD codes used in the KAERI bundle benchmarks are STAR–CCM+, ANSYS CFX, TrioCFD and OpenFOAM. Both RANS turbulence models and Large Eddy Simulation were used to simulate flow turbulence in the rod bundles. The mesh type adopted are tetrahedral, polyhedral, Hexa–dominant or hybrid (tetra+hexa). The total number of computational cells varied between 8 million (minimum) and 280 million (maximum).

The CFD results for the flow mixing in regular rod bundle (P/D = 1.35) showed a good agreement with the experimental data for the mean velocity field, while reporting large under–prediction for the RMS (root–mean–square) velocity. The CFD results for the flow mixing in tight lattice rod bundle (P/D = 1.08) showed considerable under–predictions for both the mean and RMS velocities. Analysis of the results for the flow–mixing benchmark evidences that the quality of the computational mesh has largest effect on the solution, which is not unexpected but further enhanced in this benchmark by the presence of small support structures between rods and spacers, which enhance the turbulence levels. The combination of fine hexa–dominant mesh with the Realizable k–ε(–R) model clearly produces best results for this isothermal benchmark.

The CFD results for the thermal benchmark showed a good agreement of rod temperature near the mixing–vane grid but a large discrepancy with the experimental results further downstream of the vane grid. The flow predictions dominate the accuracy in predicting the temperature distributions. The combination of a fine mesh (either hexa–dominant or fine polyhedral) and the k–ω–SST model produces best temperature predictions.

The isothermal bundle benchmark conclusions can be summarized as follows:

1. The CFD calculations show good agreement with the experimental data for the mean velocity field (axial & lateral velocity), while noticeably under–predicting the RMS (root–mean–square) velocity in regular bundle (P/D = 1.35). Limitations in the RANS method and unsteady shedding in the experiments could be responsible for the observed disagreement.

2. The CFD calculations considerably under–predict the mean axial velocity and over–predict the mean lateral velocity in tight lattice bundle (P/D = 1.08). The CFD calculations also show RMS velocity values that are significantly lower than the experimental results in tight lattice bundle. For the tight lattice geometry, in addition to

the limitations discussed in one, large scale flow pulsations could also be introduced by the tight lattice configuration and may be evaluated in the future.

3. The quality of the computational grid, in combination with the solution methods, has largest effect on the solution. Combination of fine Hexa–dominant meshes with the Realizable k–ε model clearly produces best results, which is consistent with existing guidelines. Results presented for this case will further be assessed in the future.

The thermal bundle benchmark conclusions can be summarized as follows:

1. The CFD calculations show reasonably accurate predictions of circumferential wall temperatures immediately downstream of the grid spacer, but evidence larges disagreement further downstream ($z/D > 1.5$). The discrepancy between the CFD calculations and the experiment is larger in tight lattice bundle than the for the case of a regular bundle.

2. The CFD calculations provide reasonable predictions of the heat transfer enhancement by the twist–vane grid. For the regular bundle, the BARC and CEA results show good agreement with the measured data, while the KAERI and VNIIAES calculations show large under–prediction. The KAERI predictions agree particularly well with the experimental result for the tight lattice bundle.

3. The KAERI CFD analysis demonstrated the limitations of the tetrahedral mesh approach for heat transfer predictions, while showing best results for the combination of k–ω–SST model and polyhedral+prism cells with the small dimensionless wall distance (e.g., $y^+_w = 1.5$). It is noted that the difference between turbulence models is not easy to estimate as the models are coupled to different near wall treatments. In general, the turbulence effects appear to be overwhelmed by the computational grid and near wall treatment effects.

REFERENCES

[1] ANSYS CFX User's Guide, ANSYS Inc., Canonsburg, PA, USA (2017).

[2] OpenFOAM v4 User Guide, The OpenFOAM Foundation, London, UK (2016).

[3] STAR–CCM+ Software Manual, CD–adapco Ltd., Melville, NY USA (2016).

[4] ANGELI, P.–E., BIEDER, U., FAUCHET, G., "Overview of the Trio_U code: |Main features, V&V procedures and typical applications to engineering", Proc. NURETH–16, Chicago, IL, August 30–September 4, 2015.

[5] IN, W.K. et al., Twisted Deflector for Enhancing Coolant Mixing in a Nuclear Fuel Assembly, European Patent EP 1139348, 2008.

[6] IN, W.K., SHIN, C.H., KWACK, Y.K., LEE, C.Y., "Measurement and CFD calculation of spacer loss coefficient for a tight-lattice fuel bundle", Nucl. Eng. Des. **284** (2015) 153–161.

[7] IN, W.K., SHIN, C.H., OH, D.S., CHUN, T.H., "Experimental observation and CFD prediction of flow mixing in a rod bundle with mixing vane spacer grid", 10th Pacific Symposium on Flow Visualization and Image Processing, Naples, Italy, 15-18 June 2015.

[8] LEE, C.Y., IN, W.K., LEE, J.K., "Augmentation of single-phase forced convection heat transfer in tightly arrayed rod bundle with twist-vane spacer grid", Experimental Thermal and Fluid Science, **76** (2016) 185-192.

[9] ELECTRIC POWER RESEARCH INSTITUTE, "Computational Fluid Dynamics Benchmark of High Fidelity Rod Bundle Experiments: Industry round Robin Phase 1 – Rod Bundle with Simple Support Grids", Palo Alto, CA: 2014. 3002000504. 8.

[10] ELECTRIC POWER RESEARCH INSTITUTE "Computational Fluid Dynamics Benchmark of High Fidelity Rod Bundle Experiments: Industry round Robin Phase 2 – Rod Bundle with Mixing Vane Grids", Palo Alto, CA: 2015. 3002005401.

[11] BAGLIETTO, E., "Anisotropic Turbulence Modeling for Accurate Rod Bundle Simulations", Proc. Int. Conf. on Nuclear Engineering (ICONE–14), Miami, USA, 2006.

[12] BREWSTER, R., CARPENTER, C., VOLPENHEIN, E., BAGLIETTO, E., SMITH, J., "Application of CD–adapco Best Practices to Nestor Omega MVG Benchmark Exercises Using STAR–CCM+", the 16th International Topical Meeting on Nuclear Reactor Thermal Hydraulics (NURETH–16), Aug. 30–Sept. 4, Chicago, USA, 2015.

[13] REHME, K., "The structure of turbulence in rod bundles and the implications on natural mixing between the subchannels," Int. J. Heat and Mass Transfer, **35** 2 (1992) 567.

[14] KRAUSS, T., MEYER L., "Experimental investigation of turbulent transport of momentum and energy in a heated rod bundle," Nuclear Eng. Des., v.180, 185 (1998).

[15] IN, W. K., CHUN, T. H., "Assessment of the RANS turbulence models for a turbulent flow and heat transfer in a rod bundle," Nuclear Technology, v.150, 231 (2005).

ABBREVIATIONS

ABS	acrylonitrile butadiene styrene
CFD	computational fluid dynamics
CRP	coordinated research project
CHF	critical heat flux
DES	detached eddy simulation
FEP	fluorinated ethylene propylene
LES	large eddy simulation
LDV	laser doppler velocimetry
NPP	nuclear power plant
OFEL	omni flow experimental loop
PIV	particle image velocimetry
PTS	pressurized thermal shock
PWR	pressurizzed water reactor
RANS	Reynolds averaged Navier–Stokes
RMS	root mean square
RSM	Reynolds stress model
SST	shear stress transport
WCR	water cooled reactor

CONTRIBUTORS TO DRAFTING AND REVIEW

Bieder, U.	Commissariat à l'ènergie atomique et aux ènergies alternatives (CEA), France
Hoehne, T.	Helmholz Zentrum Dresden Rossendorf (HZDR), Germany
In, W.K.	Korean Atomic Energy Research Centre (KAERI), Republic of Korea
Krause, M.	International Atomic Energy Agency
Li, Z.	Nuclear Power Institute of China (NPIC), China
Maheshwari, N.K.	Bhabha Atomic Research Centre (BARC), India
Podila, K.	Canadian Nuclear Laboratories (CNL), Canada
Smith, B.	Goldsmith Transactions, Switzerland
Starodubtsev, M. Volkov, V,	All-Russian Research Institute for NPP Operation (VNIIAES), Russian Federation
Xiong, J.	Shanghai Jiao Tong University (SJTU), China

Research Coordination Meetings

1st RCM: Vienna, Austria, 17–19 July 2013

2nd RCM: Vienna, Austria, 11–13 February 2015

3rd RCM: Daejeon, Republic of Korea, 17–19 October 2016

4th RCM: Vienna, Austria, 7–10 November 2017

IAEA
International Atomic Energy Agency

No. 26

ORDERING LOCALLY

IAEA priced publications may be purchased from the sources listed below or from major local booksellers.

Orders for unpriced publications should be made directly to the IAEA. The contact details are given at the end of this list.

NORTH AMERICA

Bernan / Rowman & Littlefield

15250 NBN Way, Blue Ridge Summit, PA 17214, USA
Telephone: +1 800 462 6420 • Fax: +1 800 338 4550
Email: orders@rowman.com • Web site: www.rowman.com/bernan

REST OF WORLD

Please contact your preferred local supplier, or our lead distributor:

Eurospan Group

Gray's Inn House
127 Clerkenwell Road
London EC1R 5DB
United Kingdom

Trade orders and enquiries:

Telephone: +44 (0)176 760 4972 • Fax: +44 (0)176 760 1640
Email: eurospan@turpin-distribution.com

Individual orders:

www.eurospanbookstore.com/iaea

For further information:

Telephone: +44 (0)207 240 0856 • Fax: +44 (0)207 379 0609
Email: info@eurospangroup.com • Web site: www.eurospangroup.com

Orders for both priced and unpriced publications may be addressed directly to:

Marketing and Sales Unit
International Atomic Energy Agency
Vienna International Centre, PO Box 100, 1400 Vienna, Austria
Telephone: +43 1 2600 22529 or 22530 • Fax: +43 1 26007 22529
Email: sales.publications@iaea.org • Web site: www.iaea.org/publications

20-01333E

International Atomic Energy Agency
Vienna
ISBN 978–92–0–106820–0
ISSN 1011–4289